MASTERARBEIT | MASTER'S THESIS

Titel | Title

On interferometric imaging of cool red giants with MATISSE

verfasst von | submitted by

Amanda Kostroun BSc

angestrebter akademischer Grad | in partial fulfilment of the requirements for the degree of

Master of Science (MSc)

Wien | Vienna, 2024

Studienkennzahl lt. Studienblatt | Degree programme code as it appears on the student record sheet:	UA 066 861
Studienrichtung lt. Studienblatt | Degree programme as it appears on the student record sheet:	Masterstudium Astronomie
Betreut von | Supervisor:	Univ.-Prof. Mag. Dr. Franz Kerschbaum
Mitbetreut von | Co-Supervisor:	Ass.-Prof. i. R. Dr. Josef Hron

Abstract

AGB stars are old, cool, luminous stars, that harbour a C-O core surrounded by a Helium- and a Hydrogen-burning shell. In this evolutionary stage pulsations, thermal pulses and stellar winds occur, leading to significant mass-loss rates. As a consequence of the strong winds, the circumstellar environment is filled with gas and dust, giving rise to various morphological structures.

In this work the object of interest is the carbon-rich AGB star R Sculptoris (R Scl). It is surrounded by a circumstellar envelope (CSE), which has already been examined in several previous papers. Among other things, ALMA revealed a spiral structure when observing in the radio regime, while the HST revealed a clumpy structure at optical wavelengths. Several studies conducted at different wavelengths (especially in the infrared) tried to reconstruct images from interferometric obervational data to obtain the shape and the composition of the CSE of R Scl.

The aim of this work is to reconstruct interferometric VLTI/MATISSE observational data of R Scl in the near-IR LM-band. Therefore three different image reconstruction algorithms are used: SQUEEZE ([BMK10]), MiRa ([Thi08]) and IRBis ([HWS14]).

The results obtained by these different algorithms shall be used to investigate the possibility of reconstructing AGB stars and their CSE, the influence of different reconstruction methods on the outcome and to verify the results obtained by Drevon et al. ([DMC+22]).

Kurzfassung

AGB Sterne sind alte, leuchtkräftige Sterne mit einer niedrigen Oberflächentemperatur, in deren Zentrum sich ein C-O-Kern, umhüllt durch eine Helium- und eine Wasserstoff brennende Schale befindet. In dieser Evolutionsphase treten Pulsationen, Thermische Pulse und stellare Winde auf, die zu einem starken Massenverlust führen. Verursacht durch starke stellare Winde wird die zircumstellare Umgebung mit Gas und Staub gefüllt, was zu verschiedensten Strukturen führt.

Das in dieser Arbeit betrachtete Objekt ist der kohlenstoffreiche AGB Stern R Sculptoris (R Scl). Er ist umgeben von einer zircumstellaren Hülle (CSE), die bereits in zahlreichen wissenschaftlichen Publikationen erforscht wurde. Unter anderem hat das Radioteleskop ALMA eine Spiralstruktur offenbart, während das HST eine klumpenartige Struktur der Hülle im optischen Bereich gezeigt hat. Einige Studien haben versucht die Hülle von R Scl im infraroten Wellenlängenbereich durch interferometrische Beobachtungsdaten zu rekonstruieren, um ihre Form und Zusammensetzung zu erforschen.

Das Ziel dieser Arbeit ist es interferometrische Beobachtungsdaten von R Scl, gemacht mit dem VLTI/MATISSE Instrument im nahen Infrarotwellenbereich (LM-band), zu rekonstruieren. Dafür wurden drei Rekonstruktionsalgorithmen genutzt: SQUEEZE ([BMK10]), MiRa ([Thi08]) und IRBis ([HWS14]).

Die Ergebnisse, die mit diesen unterschiedlichen Rekonstruktionsmethoden berechnet wurden sollen dann verwendet werden, um die Möglichkeit der Rekonstruktion von AGB Sternen und deren CSE zu untersuchen und der Einfluss der verschiedenen Algorithmen of das Ergebnis disskutiert werden. Weiters soll das Ergebnis von Drevon et al. ([DMC+22]) mit den eigenen Berechnungen überprüft werden.

Acknowledgements

I would especially like to thank my supervisors Dr. Franz Kerschbaum and Dr. Josef Hron, for their advice and patience, for answering all my questions, giving me feedback and supporting me during the work of my master-thesis.

Special thanks also to my colleague Vlad Răstău for his feedback sessions, comments and editing help.

I am very grateful for the input, discussions and help from J. Drevon, L. Planquart, C. Paladini, F. Lykou, K.-H. Hofmann and M. Mečina.

I also could not have undertaken this journey without the huge support from my family and friends, especially Andreas Pfundner, who unconditionally believes in me and encourages me to finish my study, so here I want to thank for your great support.

The results of this thesis are based on public data released from the MATISSE commissioning observations at the VLT Interferometer under Programme ID 60.A-9257(E), provided by J. Drevon in reduced form.

This research made extensive use of the Jean-Marie Mariotti Center (JMMC) tools to prepare this work, especially the `OImaging` service [1] part of the European Commission's FP7 Capacities programme (Grant Agreement Number 312430) and the `OIFits Explorer` service [2], as well as of the AMHRA `OIFits modeler` [3], which is developed by a working group of MOIO/JMMC and is supported by the Observatoire de la Côte d'Azur (OCA) through the DOMINO expertise center. MOIO is a French AA-ANO5 SNO supported by CNRS-INSU.

[1] Available at http://www.jmmc.fr/oimaging
[2] Available at http://www.jmmc.fr/oifitsexplorer
[3] Available at https://amhra.oca.eu/AMHRA/oifits-modeler/input.htm

Contents

List of Tables

List of Figures

1. INTRODUCTION

Interferometry is a very powerful observing technique. By collecting light from different telescopes and interfering their signals one can produce an interference pattern, and then analyse it in order to reconstruct the observed object. Therefore, image reconstruction tools based on different methods and algorithms are used. One key aspect of interferometric images is that they are reconstructions of the interference signal, hence they will not necessarily produce the same result as observations done with conventional single-dish telescopes (i.e. CCD cameras). In other words, the resulting images are approximations of the real objects.

In Chapter 1, a quick overview of AGB evolution is given, as well as previous research about R Sculptoris is discussed. Chapter 2 summarises the principles of interferometry, while the basics of image reconstruction is described in Chapter 3. Chapter 4 presents the available data that are used for image reconstruction and analysed in Chapter 5. The last Chapter (Chap. 6) summarises the results.

1.1. Stellar evolution of low-mass stars - in a nutshell

Depending on the initial stellar mass M_{init}, stars evolve differently after reaching the end of their hydrogen-core-burning phase. The different phases of stellar evolution and their tracks are shown in the Herzsprung-Russel diagram (see Figure 1.1).

Low-mass stars ($M_{\text{init}} \leq 2.3\ M_{\odot}$)([KWW13]), like the sun, will leave the main sequence (MS) after hydrogen is depleted in the stellar core, growing a helium core inside a burning hydrogen shell. In this so-called subgiant phase the helium core, which is degenerated, is far from igniting. After the core has grown enough and starts contracting, the hydrogen rich envelope will expand. The star moves to the red giant branch (RGB). During this phase the luminosity depends almost only on the core mass: with increasing core mass the luminosity rises. The outer convective zones grow inward, reaching the inner layers and mixing up products of nuclear reactions onto the surface of the star. This process is called the first dredge-up. At the tip of the RGB the central helium core reaches $\sim 10^8$ K, the ignition temperature of helium, and helium burning sets in. Since the helium burning in the degenerated core is unstable this leads to a thermal runaway, the helium-flash. After this fast, violent process the core helium fusion becomes stable and the degeneracy is finally removed. The following evolutionary stage is the horizontal branch phase, during which a carbon-oxygen (C-O) core is produced.

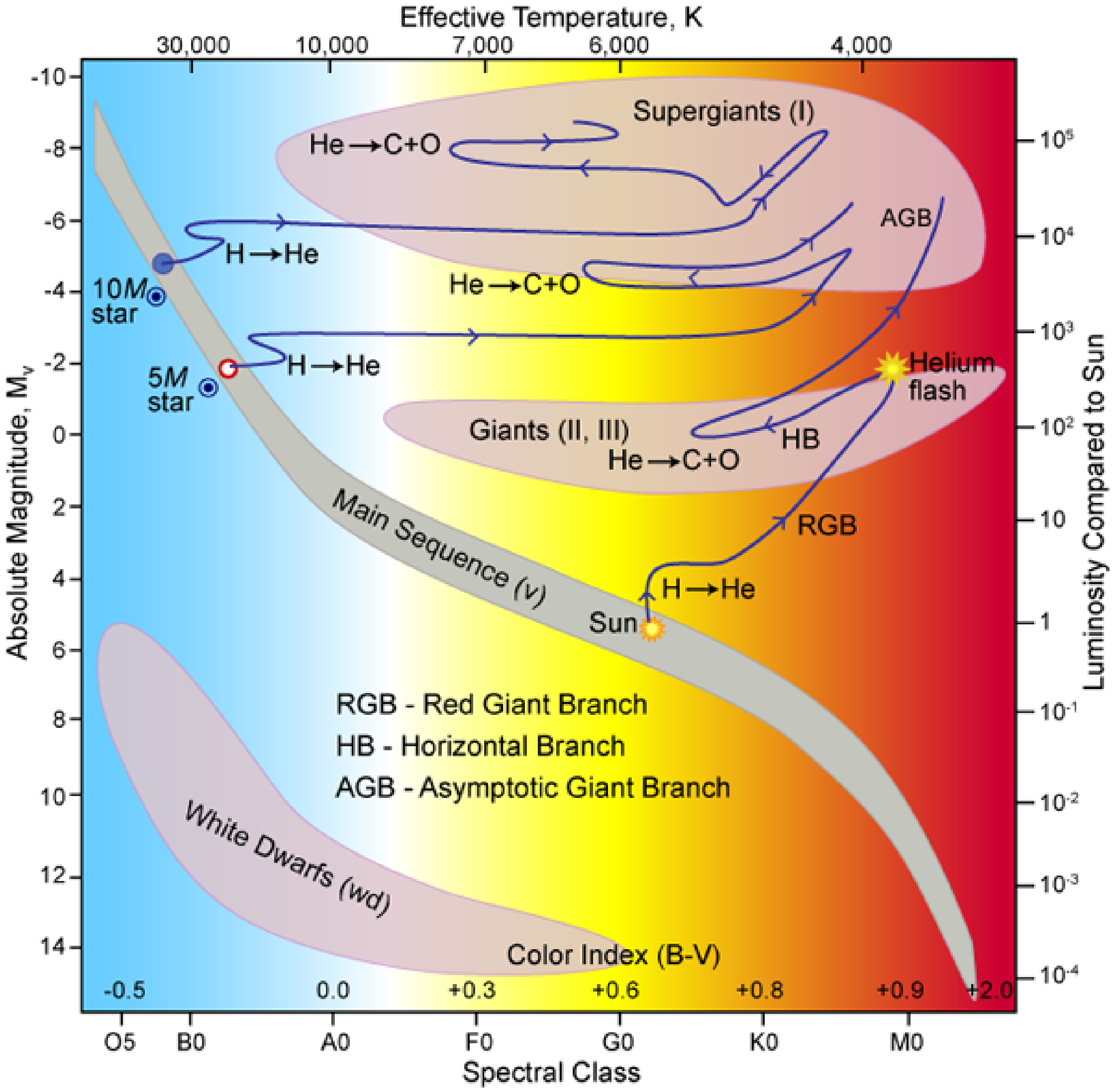

Figure 1.1.: Herzsprung-Russel Diagram,showing tracks for stars with M_{init} of 1 $M_{\odot}$, 5 $M_{\odot}$ and 10 $M_{\odot}$. ([Wie09])

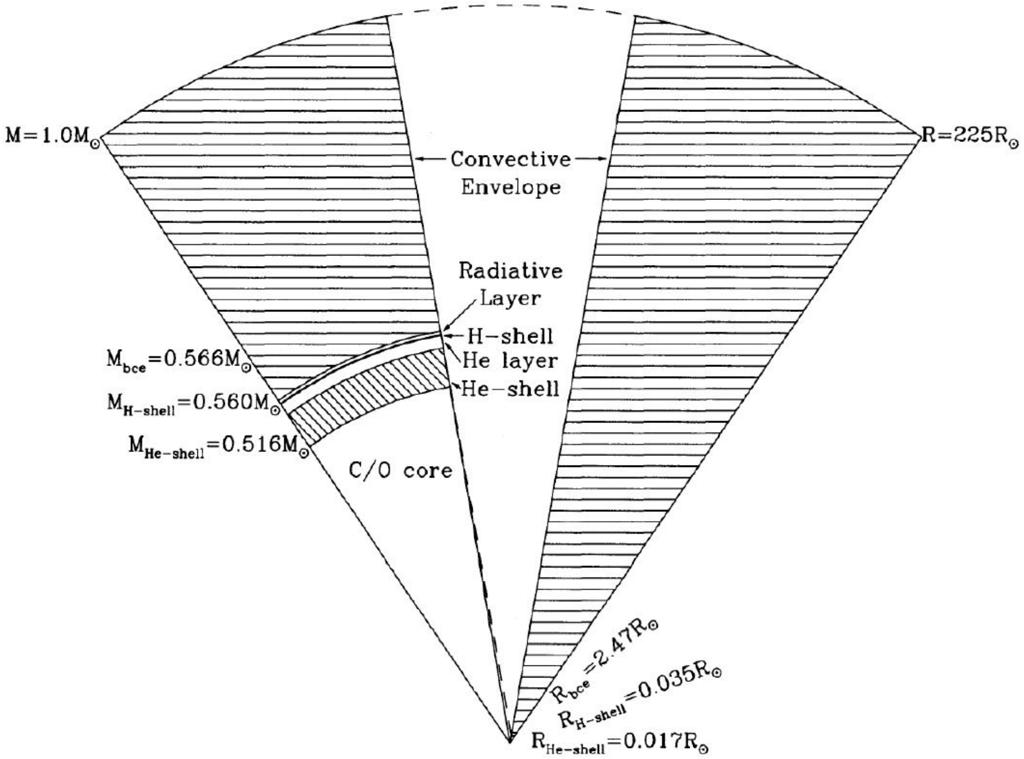

Figure 1.2.: Structure of the different layers in a 1 $M_{\odot}$ AGB star. *left side:* in mass fraction, *right side:* in radial proportions. ([HO04])

When the helium in the core is exhausted the asymptotic giant branch (AGB) is reached, the star now consist of a C-O core surrounded by a helium burning shell, which in turn is surrounded by a hydrogen burning shell (see Figure 1.2).

In this phase dredge-ups occur, where material produced in the center is mixed up towards the surface of the star. Depending on the elements appearing in the top layers of the stellar atmosphere due to dredge ups, AGB stars are categorized into three different types: M-, S- and C-type AGB stars. While there is still an excess of oxygen (C/O < 1) the stars are classified as M-type stars and their atmospheres show signatures of H_2O, SiO and TiO. Further dredge-ups continuously raise the amount of carbon in the outer layers, changing the star to a S-type star that typically possess C/O-ratios of C/O ≤ 1. Hence, S-type stars are assumed to be an intermediate step between M- and C-type stars. With an increasing excess of carbon (C/O > 1), so-called carbon-stars (C-type) result, and molecules such as CN, C_2, HCN or C_2H_2 are formed in the extended atmosphere.([HO18],[HO04])

Since AGB stars are variable in nature, by measuring the change in brightness, through the usage of light curves (e.g. see Figure 1.4), one can classify variable stars in four main categories (see Table 1.1.)

variable type	visual amplitude	period
Mira-like	large (> 2.5 mag)	regular
semi-regular (SRa)	medium (< 2.5 mag)	largely regular
semi-regular (SRb)	medium (< 2.5 mag)	poor regularity
irregular	small	irregular

Table 1.1.: Different types of variable stars ([HO04])

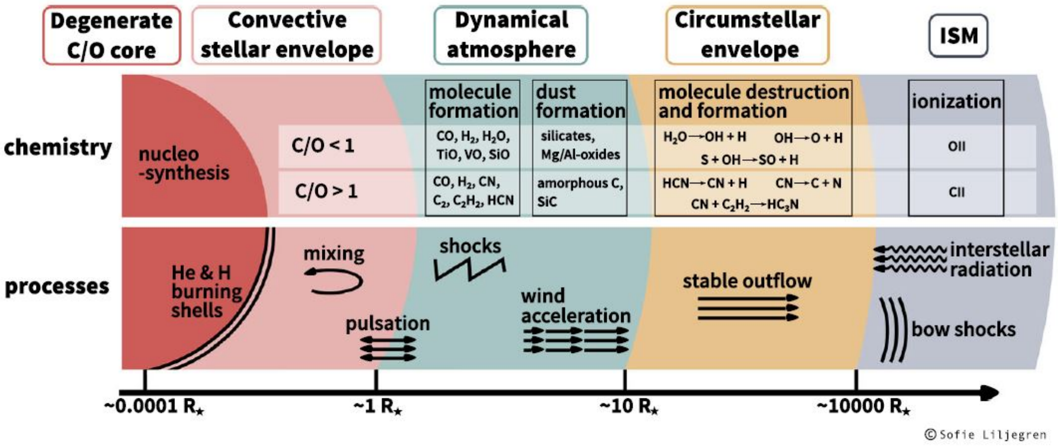

Figure 1.3.: Processes that occur in the stellar environment and effects the stellar winds of an AGB star. ([HO18])

During the AGB stage, thermal pulses (TPs), also called He-flashes, occur periodically (every $\sim 10^4$ years [HO18]). This affects the luminosity and surface temperature of the star, as the helium-shell ignites explosively after the hydrogen-burning shell has deposited enough helium on top of it. The process lasts for a few hundreds years ([HO18]), until the helim burning stops and the whole squence starts anew. ([KWW13])

It is typical for low- to intermediate-mass stars to eject gas and dust via slow stellar winds (5-30 km/s), as they get on the asymptotic giant branch (AGB). These winds are most likely driven by radiation pressure on microscopic solid-state particles, so-called dust-driven winds. A few different mechanisms, i.e. convection, pulsation, dust condensation, etc., are involved in the process. ([HO18]) In short, the gas that is present in the atmosphere of AGB stars is lifted by pulsations to heights where the temperature is cool enough (< 2000 K) and due to an increase in density this leads to condensation into dust particles, which are then pushed outwards by radiation pressure causing the surrounding gas to follow and forming an outflow that can escape the stellar gravitational field. Figure 1.3 showcases this process and the chemistry seen around AGB stars. ([HO18], [And07])

Caused by stellar winds, extended shells of dust and gas are formed, so called (detached) circumstellar envelopes (CSEs). This is very important for the evolution of the star and is a key process for enriching the interstellar medium (ISM). ([Hab96])

At the tip of the AGB the star runs out of fuel (helium) , but doesn't have enough mass to contract and start carbon fusion. Due to post-AGB super-winds the outer envelope is ejected and forms a planetary nebula (PN), containing the hot C-O core, a white dwarf (WD), as central object. The expanding circumstellar envelope cools down by moving away from the star so that more dust and a variety of different molecules form. ([KWW13])

1.2. R Sculptoris

The main object investigated in this work is the carbon-rich, semi-regular AGB star R Sculptoris (R Scl). The stellar parameters are summarized in Table 1.2. Additionally, a detached shell of gas and dust was found surrounding the star ([Olo88]).

stellar parameters

M	M_{initial}	distance	L	T_{eff}	pulsating period	$\dot{M}_{\text{present-day}}$
$[M_\odot]$	$[M_\odot]$	[pc]	$[L\odot]$	[K]	[days]	$[M_\odot/\text{yr}]$
1.3 ± 0.6	1.5 ± 0.5	370^{+100}_{-70}	4300	2640 ± 80	376	$3 \cdot 10^{-7}$
(a)	(a)	(a)	(b)	(a)	(a)	(c)

shell parameters

radius	$\dot{M}_{\text{TP}}$	TP duration	M_{dust}	M_{gas}	T	expansion velocity	age
[cm]	$[M_\odot/\text{yr}]$	[years]	$[M_\odot]$	$[M_\odot]$	[K]	[km/s]	[years]
$8.7 \cdot 10^{16}$	$2 \cdot 10^{-15}$	~ 200	$3 \cdot 10^{-6}$	$(2.5 \pm 0.5) \cdot 10^{-3}$	50	15.5	1700-2300
(b)	(c)	(e), (f)	(g)	(g), (b), (e)	(c)	(b)	(g) (c)

References: (a)[WHH$^+$17] (b)[SLO05] (c)[Mae16] (d)[DMC$^+$22] (e)[MMV$^+$12] (f)[MVB$^+$16] (g)[OME$^+$10]

Table 1.2.: Parameters of R Sculptoris

There are a few scenarios proposed regarding the formation of this shell, for example: strong mass-loss modulations during a thermal pulse (a connection between thermal pulses and detached shells have been postulated by Olofsson et al. [Olo88]) or wind-wind interactions.

The morphology of such detached shells is not yet fully understood, but there are a few leading theories behind their formation. One theory presumes that they are connected to He-flashes (thermal pulses) inside the AGB star, the shell appearing as an effect of mass-loss eruptions that interact with a previous slower wind. Another theory assumes the origin to be the interaction between the wind and the interstellar medium (ISM) through which the star is moving, producing a bow-shock structure. ([SLO05], [OME$^+$10],[Mae16])

The detached shell was observed in high detail in dust-scattered light, with the Hubble Space Telescope (HST/ACS) in 2010 by Olofsson et al. ([OME$^+$10]), using a coronographic spot to block stellar light and reveal the clumpy structure of the detached shell (see

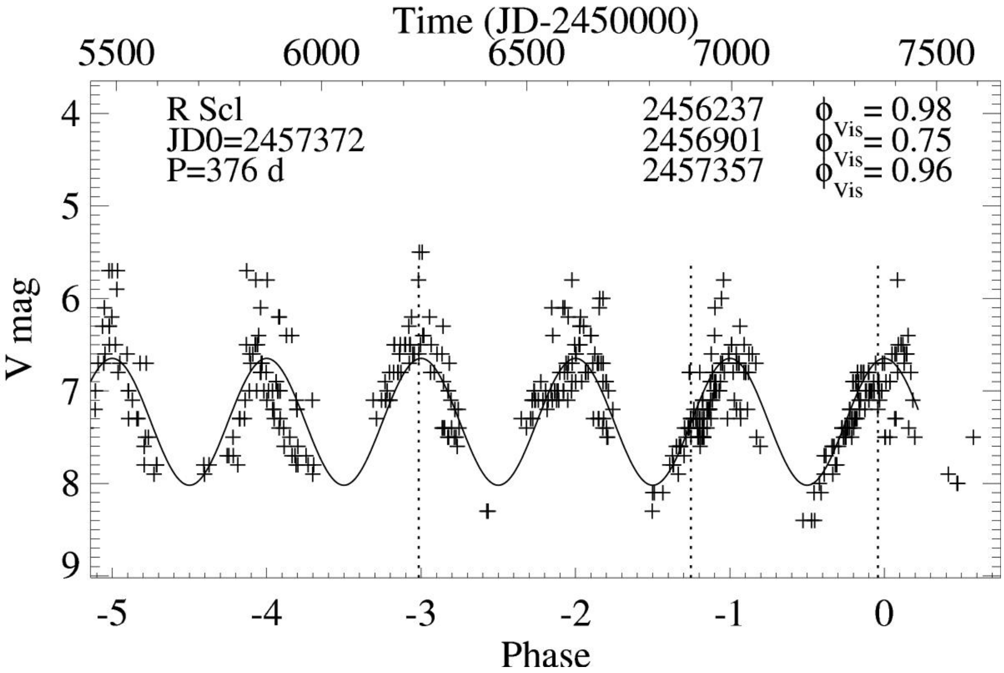

Figure 1.4.: Lightcurve of the semi-regular (SRa) AGB star R Sculptoris ([WHH+17])

Figure 1.5). A circular arc was fitted to the images, which revealed an offset of the arc in respect to the stellar position, leading to the conclusion that a binary companion might be present.

This was confirmed later by ALMA observations ([MMV+12]), the images revealing a spiral structure in the detached shell of R Scl (see Figure 1.6). Kinematic analysis estimates the age of the shell to be approximately 1800 years old and its formation is thought to be caused by a thermal pulse with a mass-loss rate ($\dot{M}$) that was 30 times higher than the pre-pulse wind. The collision, of the ejected fast material with the slower surrounding environment, shapes the outflow into its spherical shape. The spiral structure that connects the shell with the central star was then presumably formed by the binary companion interacting with the post-pulse wind. By exploring the spiral structure, such as the deviation from a perfect spiral and the contrast between the inter-winding material, one can infer certain parameters for the binary companion (M=0.25 $M_{\odot}$ [DMC+22], separation = 60 AU [DMC+22], period = 350–445 years [MMV+12] [MVB+16]). ([MMV+12], [Mae16]), [MVB+16]). To detect the binary companion itself, further observations especially in the N-band wavelength region are necessary.

Maercker et al. ([MVB+16]) differentiate the *shell* as the thin, spherically shaped gas and dust that surrounds R Scl at a distance of approximately 19.5”, and the CSE as the gas between the shell and the star.

[1] https://www.eso.org/public/images/eso1239a/

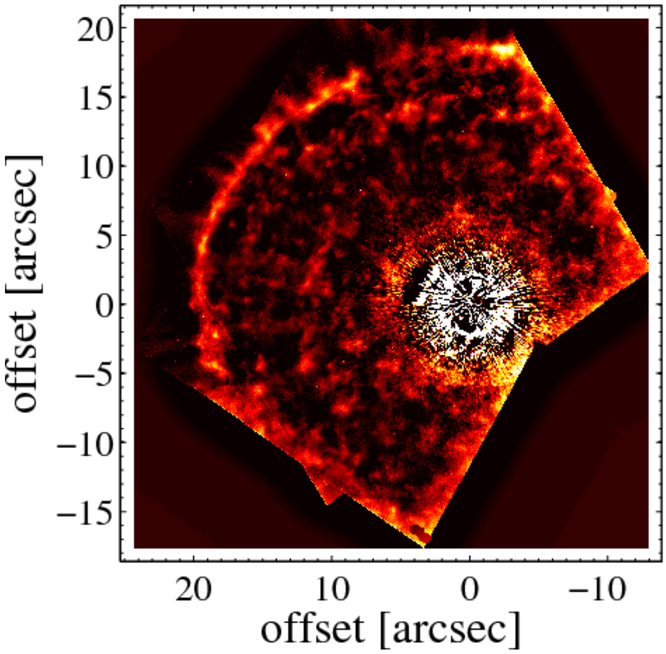

Figure 1.5.: HST/ACS images of the detached shell of R Scl ([OME+10]), revealing the clumpy structure in the CSE. A coronographic spot of 3” was used to reveal the shell-structure, leading to artifacts around the stellar position.

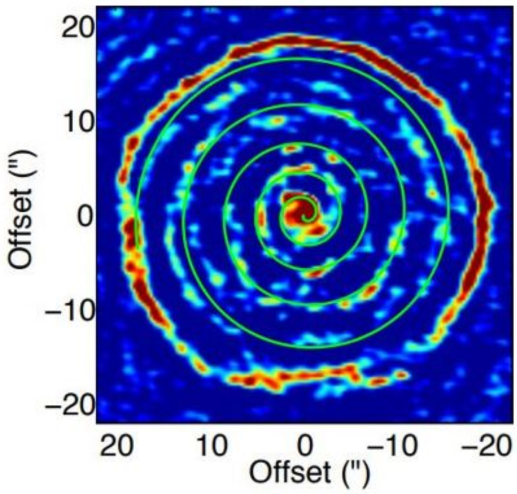

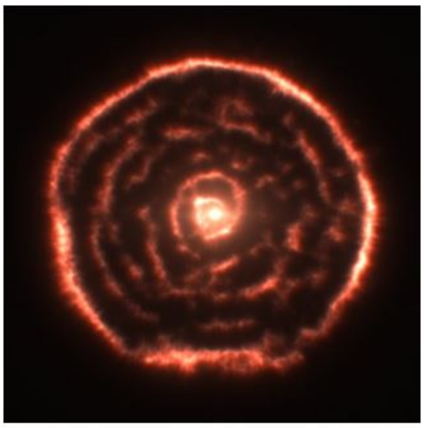

Figure 1.6.: (*left:* ALMA observations of R Scl, revealing the spiral structure ([MMV+12]), *right:* ESO ALMA data visualization of the shell and the spiral structure around R Scl (credit: ALMA (ESO/NAOJ/NRAO)/M. Maercker et al.)[1]

Drevon et al. ([DMC+22]) studied the composition of the atmosphere and close stellar environment of R Sculptoris, using IR observations obtained with the VLT interferometric instrument MATISSE ([LLP+22]). Figure 1.7 contains the SED of R Scl. The two small panels showing the LM-band and N-band wavelength-regions, that are obtained with MATISSE, revealing prominant features.

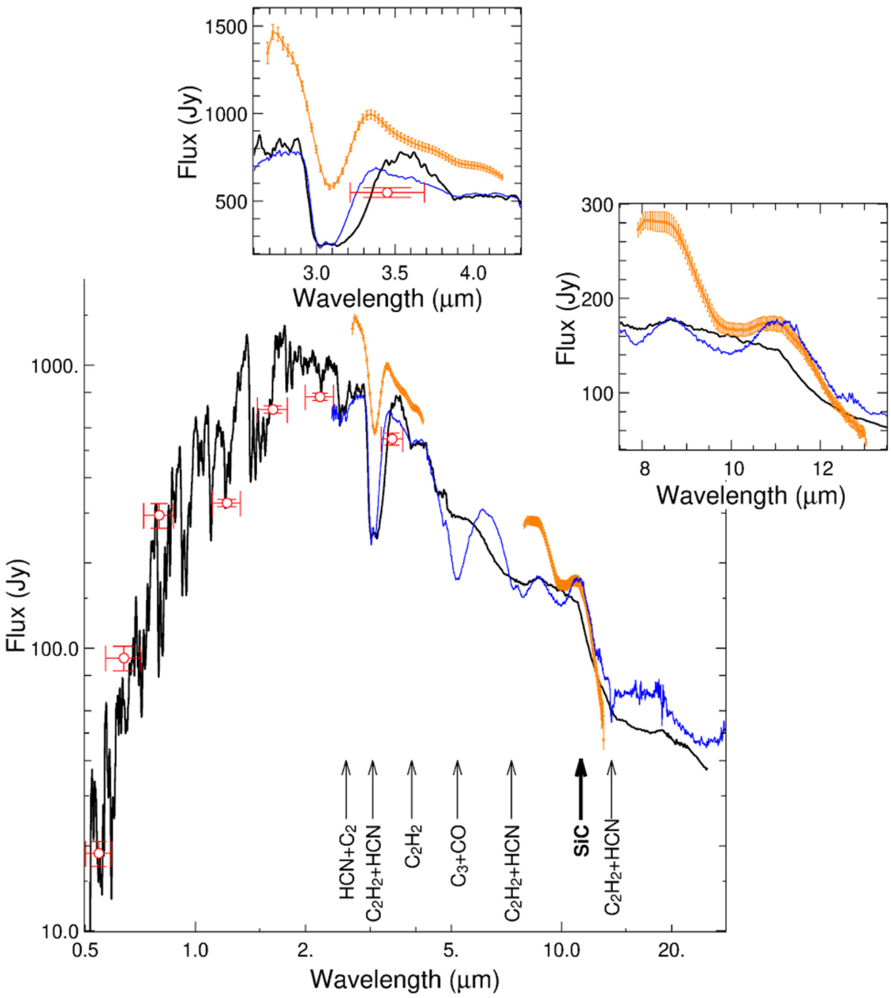

Figure 1.7.: SED of R Sculptoris. *orange:* MATISSE data, *blue:* ISO/SWS spectrum, *red:* photometric data from the literature, *black:* model from Drevon et al. 2022, *zoom panels:* on the region of the MATISSE spectra (left: LM-band, right: N-band).([DMC+22])

To estimate the composition of the CSE the 1D radiative transfere code DUSTY was used. The result is a grain composition of 88 ± 11 % amorphous carbon, AmC, while the remaining 12 ± 11 % are mainly silicon carbide, SiC, for the dust shell surrounding R Scl.

Image reconstruction was also performed as part of the study. In addition to the classical method, with MiRA, a second reconstruction tool, RHAPSODY, that reconstructs one dimensional radial intensity profiles, was used to classify different regions of the stellar environment (see Figure 1.8):

- the central part (0–1 $R_\star$, dashed blue line in fig. 1.8) was identified as the stellar photosphere. Due to molecular bands, where the photosphere is hidden, the star has different sizes at different wavelengths, showing a clear asymmetry in the 3.1 μm C_2H_2/HCN absorption band and a nearly round source in 3.52 μm.
- the innermost molecular layer (1–2 $R_\star$) extends beyond the stellar photosphere as a faint environment (see Figure 1.8 between the dashed blue line and the inner green line). This irregular extended shell that is attached to the central component is very prominent at 3.1 μm, where the SED (see Figure 1.7) reveal clear spectral features that are assigned to C_2H_2 and HCN. Hence, these two molecules (C_2H_2, HCN) form in cool, carbon-rich, stellar atmospheres, it is assumed that this molecular layer shows the extended stellar atmosphere of R Sculptoris.
- the green lines in Figure 1.8 represent the inner and outer boundary of a distinct hot molecular layer (2.3–3.4 $R_\star$). This complex layer is reconstructed in the L-band with MiRA (as a fuzzy arc in the NW-region, white arrow, and by a few blobs in the same distance), as well as with RHAPSODY (clear continuous ring). The composition of this layer is disputed: either dust (amorphous carbon, amC, silicon carbide, SiC, or titanium carbide, TiC) or molecules (C_2H_2, HCN) or both.
- the outermost layer, called fuzzy emission, (3.8–17 $R_\star$) cannot be reconstructed very well, because of the sparse uv-coverage. Nevertheless this layer is possibly indicated as blobs and artifacts in the reconstructed images.

In summary, the computations of Drevon et al. ([DMC$^+$22]) reveal clear structures in the wavelength ranges where spectral features are present. It is assumed that the innermost molecular layers contain C_2H_2 and HCN. Because these molecules form inside the stellar atmosphere one can assume that this layer is connected to the extended stellar environment, which can be seen in all L-band reconstructions, especially in 3.1 μm and 3.52 μm, as faint emission surrounding the central object.

Results, published by Wittkowski et al. in 2017 ([WHH$^+$17]), used near-IR H-band (1.5–1.8 μm) observations of the carbon star R Scl, obtained with the VLTI/PIONIER instrument in 2014. Data from three spectral channels, 1.59 μm, 1.69 μm and 1.76 μm, were reconstructed with the image reconstruction tools IRBis, MiRa and BSMEM (see Figure 1.9). The reconstructed images show the stellar disk, a complex structure including a dominant bright spot. It is assumed that newly formed amC dust clouds close to the stellar photosphere effectively block near-IR light. Hence, the bright spot is showing a region where the stellar surface of R Scl is less covered. Theoretical predictions, based on simulations, show that such structures vary within a few months. Therefore, investigations at different timesteps are needed for further clarification of the structure/clumpiness of the CSE of R Scl. Based on the data, the binary companion is not thought to influence the surface and close CSE of R Scl nor its evolution along the AGB phase.

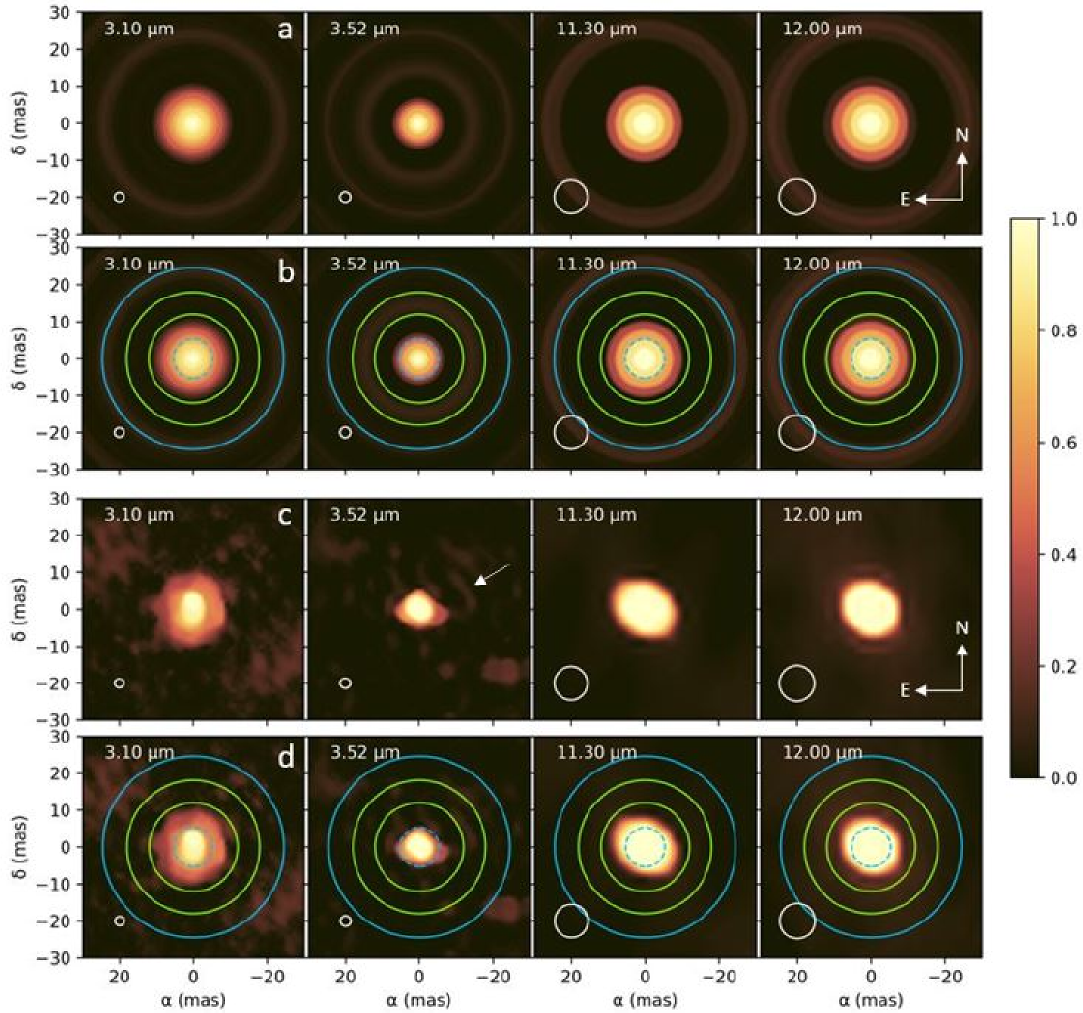

Figure 1.8.: Reconstructed images of R Scl with RHAPSODY (*top (panels a and b)*) and MiRA (*bottom (panels c and d)*) of the different wavelength ranges. In the lower panels for each reconstruction tool (b and d) the investigated environment regions are plotted onto the reconstructed images. ([DMC+22])

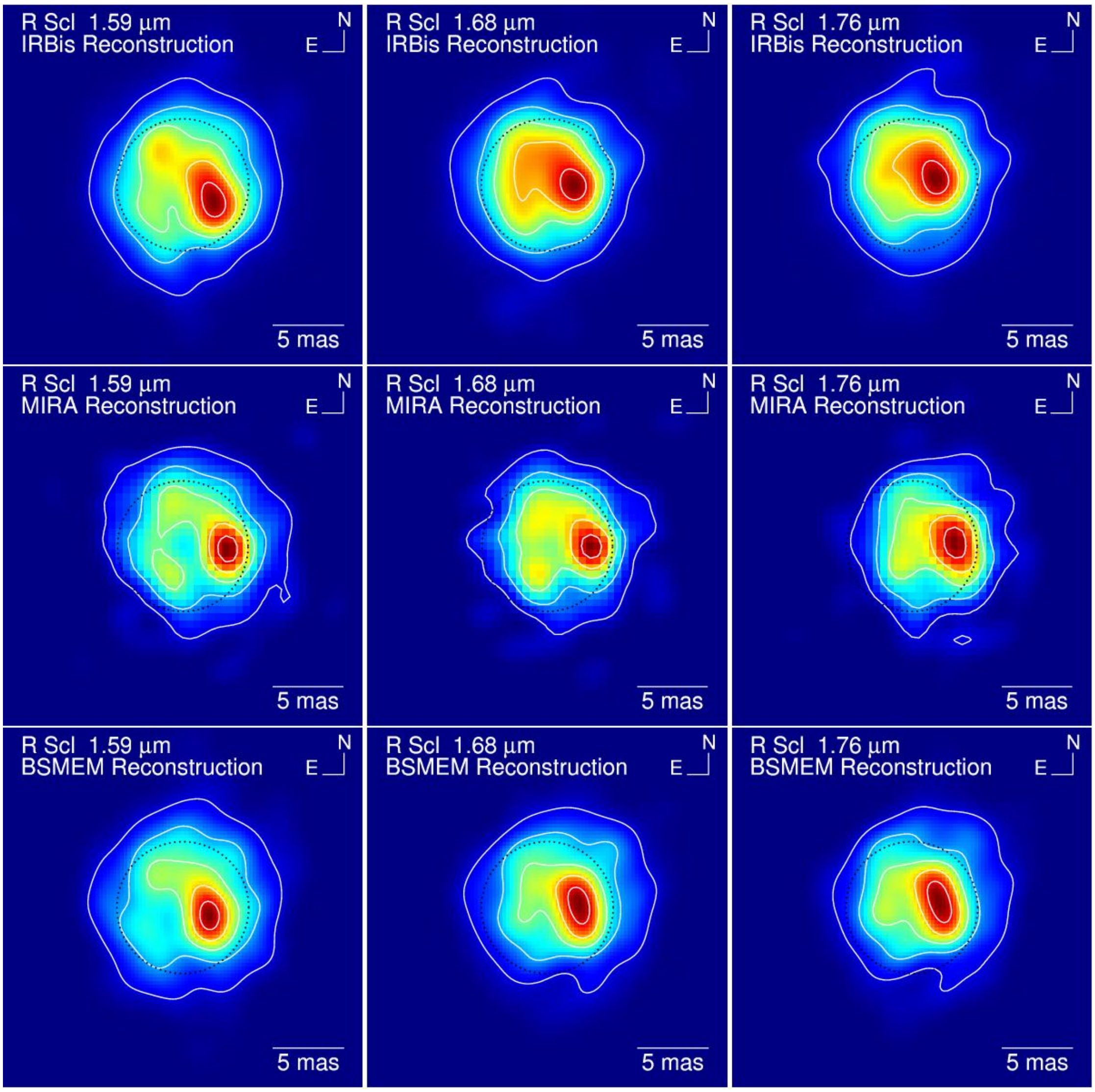

Figure 1.9.: Reconstructed surface of R Scl by Wittkowski et al.([WHH+17]), from different reconstruction tools in three wavelength-channels. IRBis (*top*), MiRA (*middle*), BSMEM (*bottom*).

1.3. The many faces of R Sculptors / Motivation

In interferometry it is common to use and compare different image reconstruction algorithms as a means of obtaining the most reliable image of an object. The results from the various methods are compared in terms of morphological structures, intensity profiles, as well as artefacts and background noise.

In this master-thesis observational data of the AGB-star R Scl, obtained by the MATISSE instrument at the VLTI, will be analysed by applying three different image reconstruction tools:

- SQUEEZE ([BMK10])
- MiRa ([Thi08])
- IRBis ([HWS14])

2. INTERFEROMETRY, TELSECOPES and INSTRUMENTS

2.1. Introduction to interferometry

Interferometry uses the wave-nature of light to combine two or more telescopes, to obtain better observational results (in particular higher angular resolution) than with single dishes. The theoretical principles of an interferometer are based on Young's two slit experiment: if a plane parallel wave from a distant point source hits an aperture with two slits, the light would be diffracted and show a sinusiodial illumination pattern (also called fringe-pattern) with an amplitude depending on the brightness of the source. A second slightly inclined lightwave will produce a slightly shifted pattern with respect to the first and the overall resulting illumination pattern will be the interferece of these two. (see Figure 2.1)

In practical interferometers this principle is realized by using two or more telescopes (representing the slits) and interfering the light from the different dishes in a beam-combiner. ([EMP23], [Mon03])

2.1.1. Resolution & Fringes

Typically interferometers have higher angular resoultion, Θ, than single dish telescopes. The *Rayleigh-Criterion* defines the resolution as Equation 2.1, which in the case of two point sources places the diffraction maximum (center) of one object to the first minimum (zero) of a second object.

$$\Theta_{\text{telescope}}[rad] = 1.22 \cdot \frac{\lambda[m]}{D[m]} \tag{2.1}$$

The *interference pattern*, also called *interference fringes*, is a pattern of alternating light and dark bands and is produced by interferometers by superimposing the light from two or more telescopes in a beam-combiner. This fringe-pattern contains a lot of information about the observed star, such as the size, shape, or brightness distribution. For interferometers a similar criterion to the Rayleigh-Criterion can be used (Equation 2.2), calling two sources resolved if the fringe contrast approaches zero at the longest baseline B. ([Mon03])

$$\Theta_{\text{interferometer}}[rad] = \frac{\lambda[m]}{2 \cdot B[m]} \tag{2.2}$$

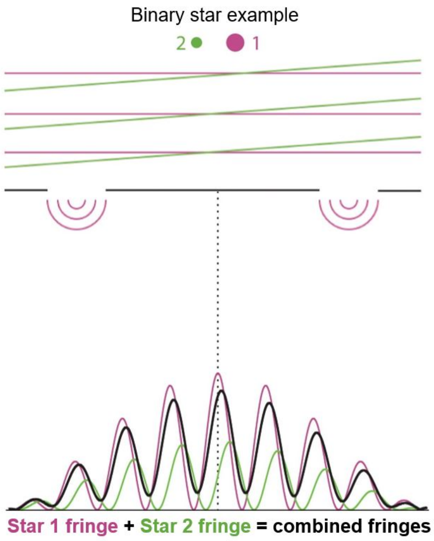

Figure 2.1.: Principle of Young's two-slit experiment showing the interference pattern of two slightly shifted point sources with different intensities (adapted from [EMP23])

2.1.2. Complex Visibility & uv-Plane

The *Complex Visibility*, $\tilde{V}$, can be measured from the interference pattern. It is composed of the fringe contrast, called the *Visibility Amplitude*, V, and the *Visibility Phase*, Φ, which contains the relative position of the fringe. For a simple two-telescope interferometer the visibility amplitude is defined by Equation 2.3, where I_{max} is the maximum intensity and I_{min} the minimum intensity of the fringes. If V=1 the interference pattern is fully-modulated and shows bright peaks and dark nulls, created by constructive and destructive interference. Otherwise, if V=0 no modulations in the fringe pattern are observable.

$$V = \frac{I_{max} - I_{min}}{I_{max} + I_min} = \frac{\text{Fringe Amplitude}}{\text{Average Intensity}} \tag{2.3}$$

The *Cittert-Zernike theorem* describes mathematically the observed complex visibility $\tilde{V}$ as a Fourier Transformation of the brightness distribution I:

$$\tilde{V} \propto \mathcal{F}(I) \tag{2.4}$$

The squared amplitude of the complex visibility (squared visibility $|V|^2$), also called the powerspectrum, is an important and well measurable observable but doesn't include information about the visibility phase.

The coordinates (u,v) span a two-dimensional plane of spatial frequencies, called the *Fourier-Plane* or *(u,v)-plane*. Each point in the (u,v)-plane corresponds to a projected

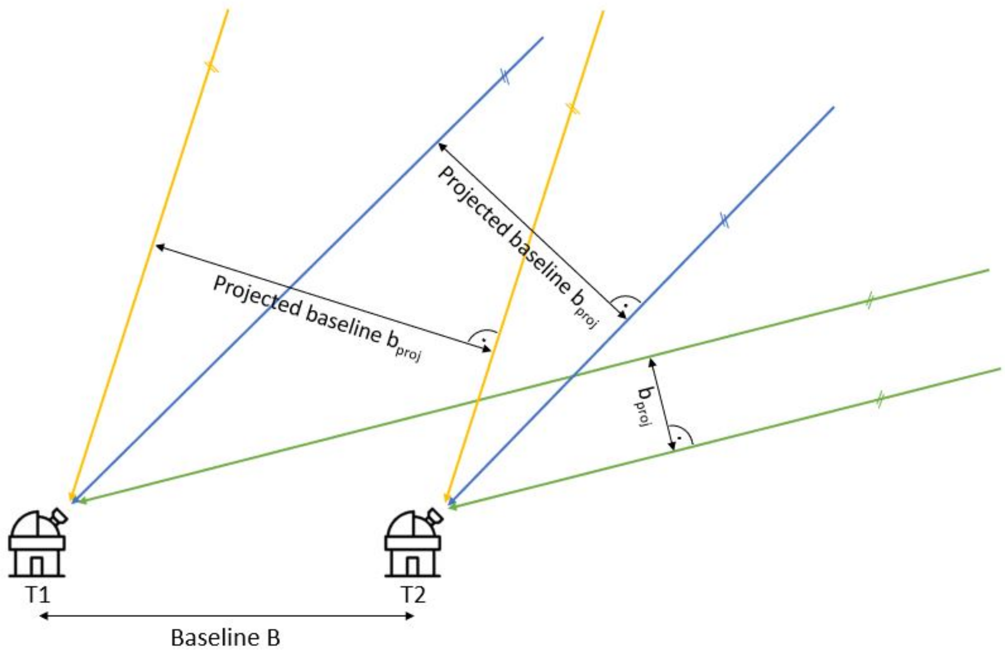

Figure 2.2.: The projected baseline b_{proj} is the relative, projected distance between two telescopes. Earth's rotation causes a movement of the objects on the sky, which changes the projected baseline over time.

baseline (see Figure 2.2) and contains complex visibility measurements. The more the (u,v)-plane is filled (higher uv-coverage), the higher quality images can be created. There are a few methods to increase the uv-coverage:

- increase the number of telescopes:
  The number of baselines in an N-telescope interferometer is defined as $N \cdot (N-1)/2$, thus a higher uv-coverage is obtained by increasing the number of telescopes.
- when Earth rotates around its axis, astronomical objects change their angle of incidence, which leads to different projected baselines (see Figure 2.2).
- some telescopes can be moved, consequently different baselines can be produced.
- data from interferometers at different geographical locations can be combined to improve the uv-coverage.
- special case: Achromatic objects, that do not depend on the wavelength, offer higher uv-coverage.

Figure 2.3 shows how the number of telescopes and also how Earth's rotation influence the uv-coverage. ([EMP23],[Mon03])

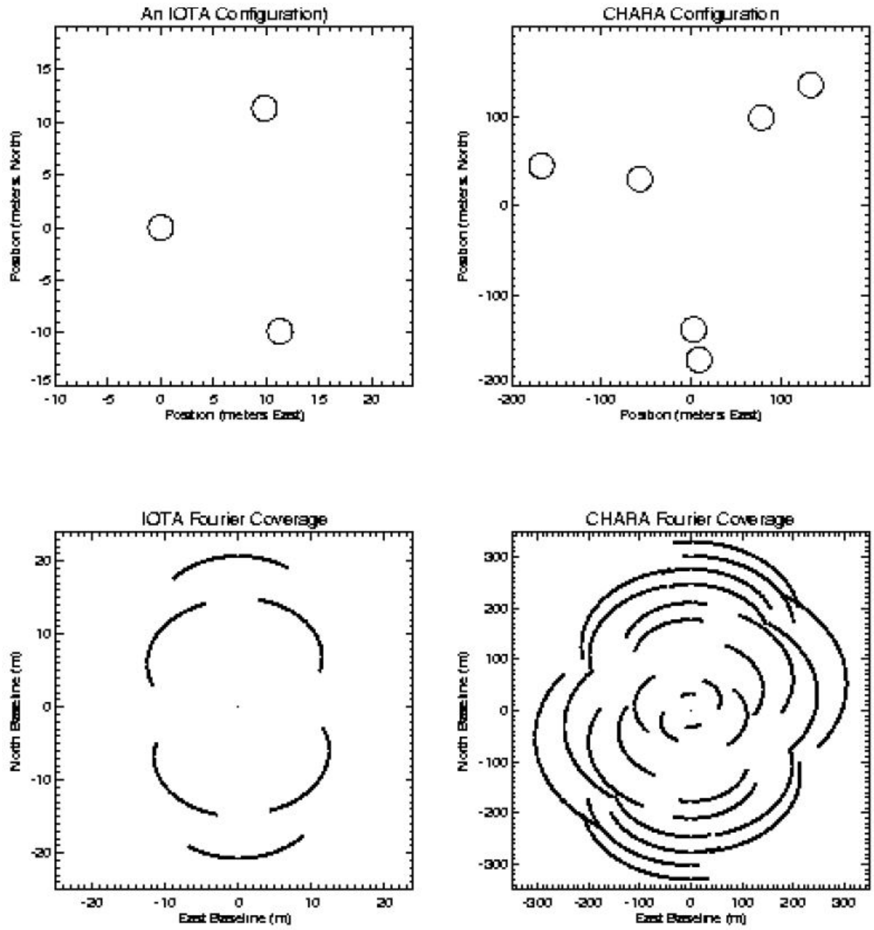

Figure 2.3.: Different telescope configurations (top panels) cause different uv-coverages (bottom panels). The interferometer observes over a period of 3 hours, which leads, due to Earth-rotation, to a bigger uv-coverage and shows up as lines in the uv-coverage. (adapted from [Mon03])

2.1.3. Atmospheric Turbulence & Closure Phase

Due to our atmosphere, things such as atmospheric density, temperature, humidity and other variations lead to different path lengths and a disturbed wavefront incoming at the interferometer. To quantify these distortions different parameters are introduced:

- the Fried parameter, r_0, (coherence length) is defined as the distance over which a wavefront remains unperturbed ($< \lambda/2.4$ ($\sim$1 rad)). Hence, it provides an upper limit for the useful size of the single aperture.

- coherence time, t_0, (see Equation 2.5) is the time over which atmospheric perturbations are assumed to be constant, hence it provides a wavelength dependent limit for the timescale over which corrective methods need to operate.

$$t_0 = \frac{r_0(\lambda)}{v_{wind}} \tag{2.5}$$

- since atmospheric turbulences vary across the sky, the *isoplanatic angle*, Θ_0, is defined as the angle of separation between two objects in order for them to go through the same turbulent region. Its size is dependent on the height at which turbulences occur in the atmosphere and the observed wavelength λ, i.e. the angle becomes larger the lower the atmospheric height and that longer the wavelengths. As a reference, the isoplanatic angle is of the order of a few arcseconds in the visible wavelength range and on the arcminute scale in the near-infrared.

Atmospheric turbulence above each telescope generate wavefront time delays, which are seen as phase shifts in the detected fringes. These deviations have to be corrected to receive the real phase information. To do this, the closure phase is introduced. This is a parameter that requires a minimum of three telescopes and which quantifies the visibility phases of each individual telescope at a moment in time in a way that eliminates their individuall errors (coming from atmospheric perturbances). A phase shift caused by one telescope will operate equal but opposite-signed when interfering with the other two telescopes respectively. [EMP23],[Mon03]

Another good observable in optical/IR interferometry is the bispectrum. It is composed of the powerspectrum (squared visibility) and the closure phase. Hence, it contains phase information that is insensitive to atmospheric turbulences. For more details and mathematical explanations on visibilities, powerspectra, closure phases and bispectra see e.g. the book of Glindemann ([Gli11]).

2.2. Difference between radio and optical/IR interferometry

In radio astronomy the signals from each telescope can be coherently recorded, digitized and interfered mathematically, while in optical/IR interferometry, due to the particle properties of light, the incoming light has to be physically interfered. Therefore, so-called delay-lines with numerous optical elements are used to transport, and in this correct for optical path differences, the light from the telescope to a optical laboratory where it is interfered and can then be optically measured. Additionally, the wavelength is much smaller in the optical range, so that the optical path has to be more precise.

Another important difference is that atmospheric turbulences are more significant in the optical/IR than in the radio regime.

2.3. VLTI - Very Large Telescope Interferometer

The *Very Large Telescope Interferometer* (VLTI) is one of the biggest optical/IR interferometers. It either combines the four big VLT Unit Telescopes (UTs) (mirror-diameter of 8.2 m) or the movable four Auxiliary Telescopes (ATs) (mirror-diameter of 1.8 m). Three instruments, MATISSE, GRAVITY and PIONIER are currently available and can combine light from four telescopes simultaneously. Therefore, a complex system of delay lines is built underground, to align the light-paths of all telescopes.[1]

Figure 2.4 shows the overall layout of the VLTI.

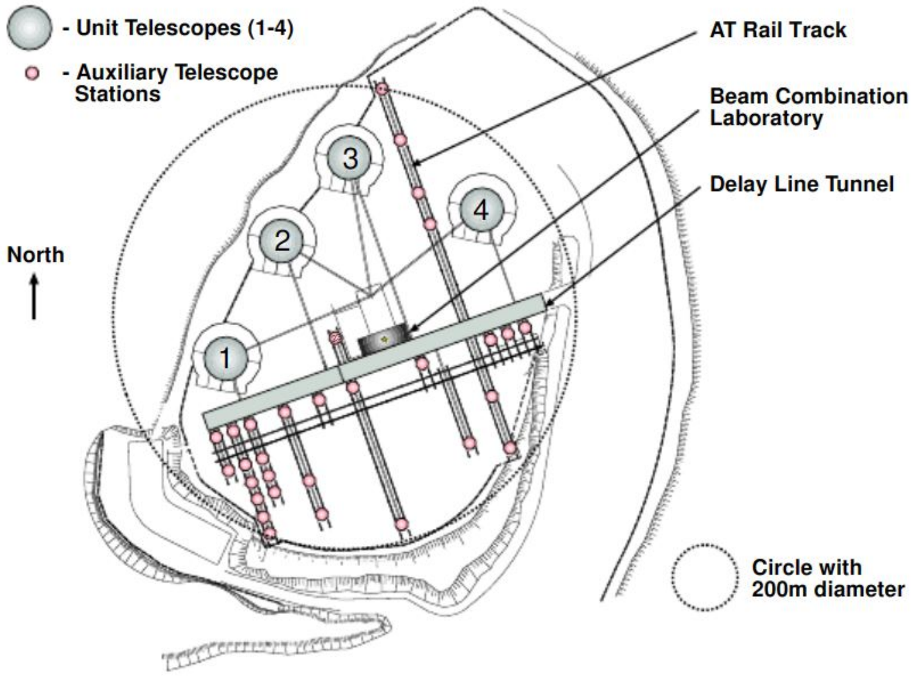

Figure 2.4.: Overall layout of the VLTI including the four UTs and the possible ATs positions along their rail tracks. ([GDK+04])

2.3.1. MATISSE

MATISSE, the *Multi AperTure mid-Infrared SpectroScopic Experiment* operates in the mid-infrared, containing three different bands (L, M and N, see Table 2.1, visualized in Figure 2.5) which can be observed simultaneously. It can operate in two different modes: global combination, where all four telescope beams produce a common interference pattern and pair-wise combination, where the telescope beams are mixed in pairs. The key-science-goals of MATISSE are to investigate disks around young stellar objects (YSOs), study the surface structures of stars, explore the mass-loss of evolved stars and binaries and to look into the environment of black holes (BHs) in active galactive nuclei (AGNs). The data used in this work were obtained during the comissioning phase of MATISSE in December 2018.

[1] https://www.eso.org/sci/facilities/paranal/telescopes/vlti.html

band	wavelength λ [μm]
L	2.8 - 4.2
M	4.5 - 5.0
N	8.0 - 13.0

Table 2.1.: IR-bands, covered by the MATISSE experiment at the VLTI ([LLP+22])

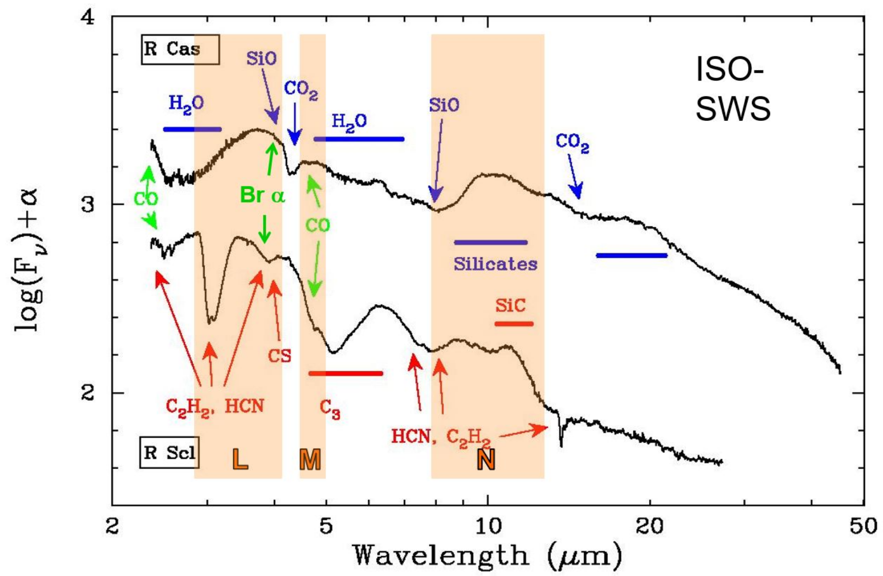

Figure 2.5.: Spectrum of the carbon star R Scl (bottom) and M-star R Cas (top) including markings of different molecular features (arrows) and the wavelength regions of the three different VLTI MATISSE bands L, M and N. (Hron, private communication)

The MATISSE instrument has a complex structure (see Figure 2.6), composed of a *warm optical system* at the entrance of the instrument that operates in ambient temperatures, and two *cold optical benches*, cooled down to 35 K. Due to different wavelength-characteristics and spectral bandwidth sensitivity the L- and M-band use a different cryostat and detector than the N-band. First, the four beams from the telescopes enter the warm optical system, where two independent beam commuting devices (BCDs)[2] are placed. Each BCD affects two beams coming from the telecopes. BCDs in 'IN' mode commute their incoming beams, while BCDs in 'OUT' mode don't influence the lightrays. Hence, four different combinations (IN-IN, IN-OUT, OUT-IN and OUT-OUT) are possible. After passing through the BCDs, the beams are spectrally seperated and pass through two modules, which cause the co-alignment between the warm and cold optics and equalise the optical path differences between the beams (delay-lines), before entering the cold optical benches. Inside the cryostats a vacuum ($< 1.10–5$ mbar) is produced and optical elements located there split the light into the interferometric and the photometric channels of the instrument. Finally, after passing the disperison elements and spectral filters, the light reaches the detector. ([LLP+22])

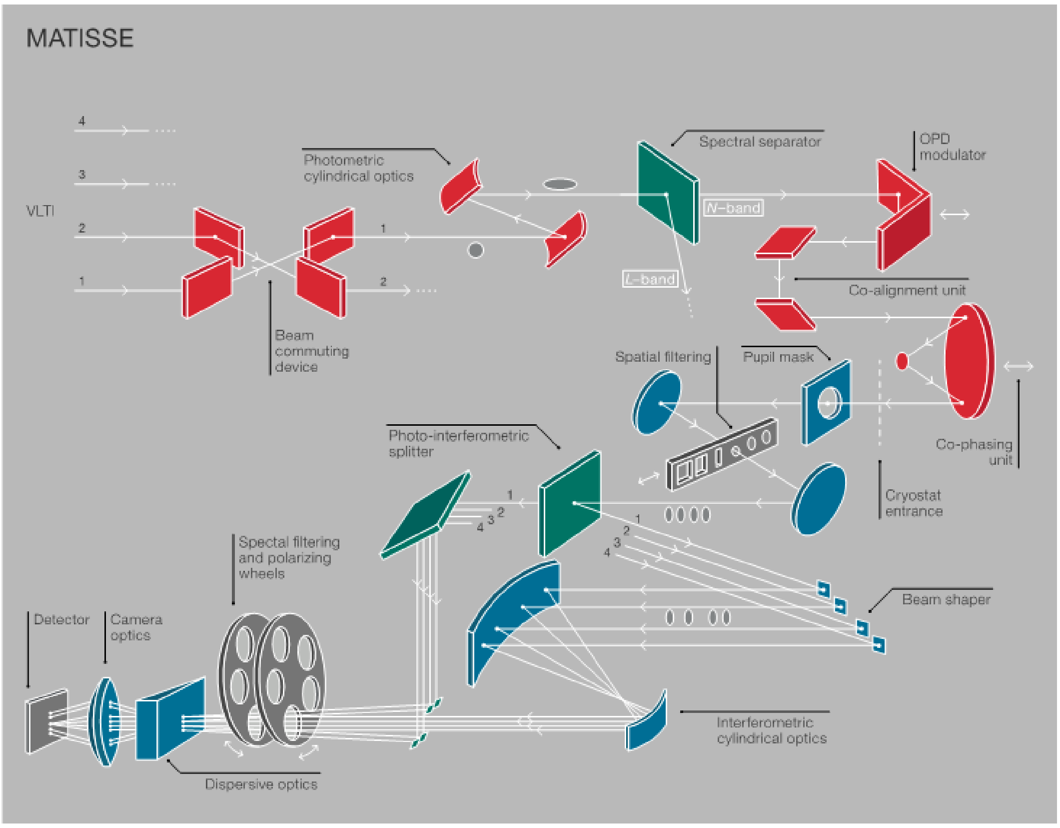

Figure 2.6.: Structure of the MATISSE instrument at the VLTI ([LLP+22])

[2]https://www.eso.org/sci/facilities/paranal/instruments/matisse/doc/template_manual.pdf

3. IMAGE RECONSTRUCTION

As a consequence of the fact that interferometers consist of two or more telescopes, separated by different baseline-lengths, the uv-plane is not fully filled (see Section 2.1.2) and hence some information is missing. To obtain an image from these sparse data, missing data has to be interpolated by using mathematical algorithms. Various methods are known, based on different techniques and approaches. It is common to apply several image reconstruction methods, so the results can be compared and verified.

3.1. Theoretical principles of image reconstruction

The theoretical mathematical principles used for image reconstructions in the optical/IR are well explained in [TY17], [RTM11], [Mon03] or [EMP23], just to name a few. As interferometric data are sparse and affected by atmospheric noise, it should not be expected that reconstructed images are completely accurate. There are many candidate images that can be estimated and may explain the observed data. To converge the algorithms to a unique and stable solution additional constraints, so called *regularizations*, have to be set to interpolate the voids in the (u,v)-plane and to select the best estimates of the true image. Due to the fact that the images are brightness distributions, the assumptions of non-negativity and normalisation are implemented by default.

The main goal of all algorithms is to find the optimal image that fits the obtained data and the defined priors best. This can be expressed in a constrained optimization problem:

$$\hat{x} = \min\Big(f_{\text{data}}(x) + \mu \cdot f_{\text{prior}}(x)\Big) = \min\Big(f(x)\Big) \tag{3.1}$$

Equation 3.1, used for image reconstructions, consists of three terms: the likelihood-term, f_{data}, compares the available data and the reconstruction, the regularization-term, f_{prior}, indicates the discrepancy with the prior constraints and the hyperparameter, μ, ($\mu > 0$) weights between the data and the priors. In short, by minimizing f_{data}, more emphasis will be placed on fitting the actual data, while minimizing f_{prior} will switch the focus of the fitting algorithm on the assumptions that are made.

Image reconstruction algorithms are solving this optimization problem iteratively, using various different optimization strategies (e.g. gradient based or stochastic methods). The gradient based method computes the gradient of the function $f(x)$ (see Equation 3.1) and minimizes it step by step. However, the stochastic method randomly guesses a new value $x^{[t+1]}$ and only uses it if the function f takes a value that is smaller than the previous step ($f(x^{[t+1]}) < f(x^{[t]})$). To avoid local minima in the search for a global solution an additional probability of keeping a higher function-value is implemented. (With this probability, the search continues even though $f(x^{[t+1]}) > f(x^{[t]})$.) This probability decreases with the difference between the two steps. If $f(x^{[t+1]}) - f(x^{[t]})$ is high the possibility of rejecting this value is also high. This procedure is called a *Monte Carlo Markov Chain* (MCMC)[1]. Compared to local optimization methods, such as the gradient based method, the converging time is much longer. However, an estimate of the errors and not just the brightness distribution (image) can also be obtained. ([TY17])

3.2. Dirty Beam & Dirty Image

Interferometric image reconstruction methods are grounded on the mathematical principles of Fourier transform. The estimate of the sensitivity of the observing configuration is called the "dirty beam" and is obtained by computing the Fourier transform of the uv-coverage. (see Figure 3.1, bottom left). The convolution of this dirty beam with a real image or an image model leads to the "dirty image" (see Figure 3.1, bottom right), that presents real features as well as artefacts that arise due to gaps in the uv-coverage. Hence, this shows artefacts and regions of higher or lower sensitivity, which then have to be taken into account when analysing the results from image reconstruction algorithms. ([TY17])

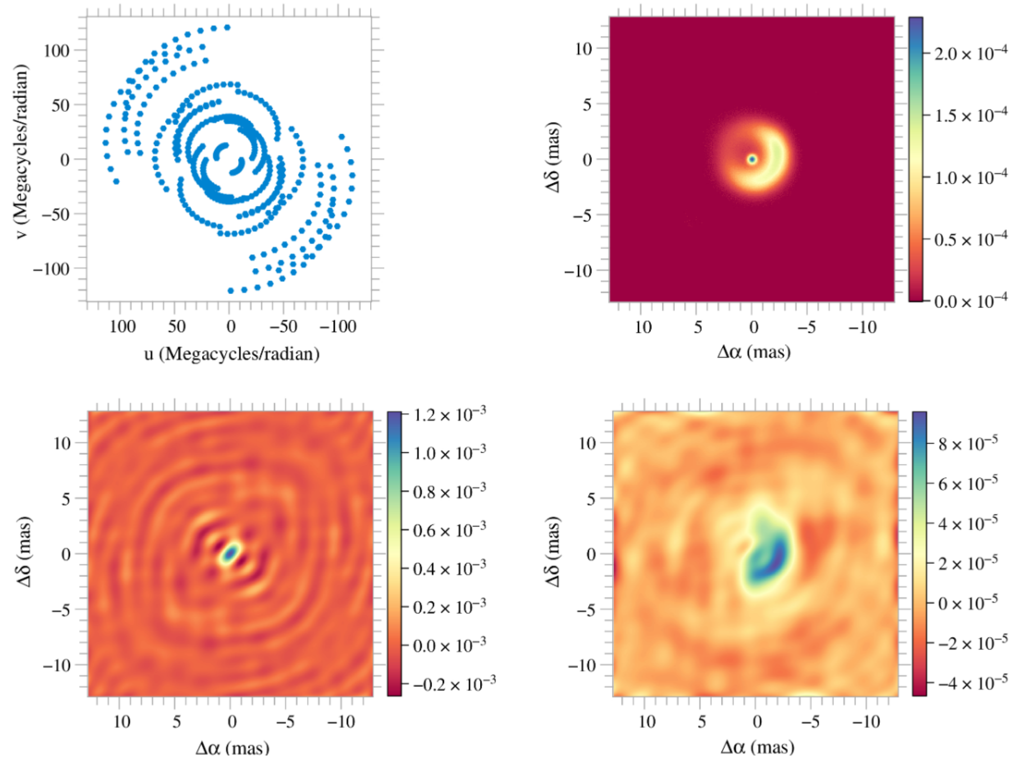

Figure 3.1.: Modeled LkHa101 observation, *top left:* uv-coverage, *top right:* Model, *bottom left:* Dirty Beam, *bottom left:* Dirty Image. ([TY17])

[1] for detailed description of the Monte Carlo algorithm see e.g. [MNR12].

3.3. Quality estimation

Reconstruction algorithms use a series of different parameters to generate images, so the results are always an estimate. Hence, the best result is usually selected based on certain quality parameters that are calculated from the generated data. The various quality parameters are described below and summarized in Table 3.1.

3.3.1. Reduced Chi2

All methods, that are used in this work, use the reduced χ^2 (CHI2r) as a quality parameter. The classical χ^2 (= datamodel^2/uncertainty^2) is normalized and hence becomes larger from a bigger dataset. Therefore, this value is additionally divided by the number of datapoints to make it model-independent. This quality parameter can also be calculated for the different parameters generated for the reconstruction, e.g. the squared visibility ($\chi^2_{V^2}$) or the closure phase (χ^2_{CP}). The best reconstruction should in principle have a reduced χ^2 as close to unity as possible.

3.3.2. Residual ratios

Another way to estimate the quality of the data can be done via the residual ratios $\rho\rho_{V^2}$, $\rho\rho_{CP}$. This ratio between the sum of all positive residuals and the sum of all negative residuals should be close to unity, to reach an equal distribution of the positive and negative residuals, and hence a good fit. ([HWS14])

3.3.3. Reconstruction quality parameter

IRBis uses both of the quality estimates listed above, combined in one new parameter, $\mathrm{q_{rec}}$, to estimate the quality of the reconstructed image:

$$\mathrm{q_{rec}} = \frac{1}{4} \cdot \left[(\chi^2_{V^2} - 1) + (\rho\rho_{V^2} - 1) + (\chi^2_{CP} - 1) + (\rho\rho_{CP} - 1) \right] \tag{3.2}$$

If χ^2 or $\rho\rho$ are smaller than one, their reciprocal values ($\frac{1}{\chi^2}$ or $\frac{1}{\rho\rho}$) are used, to prevent the existing noise from being fitted.
The better the reconstructed image, the closer the values of $\mathrm{q_{rec}}$ are to zero. ([HWS14])

quality parameter	desired value	used in
χ^2	$\rightarrow 1$	SQUEEZE, MiRA, IRBis
$\rho\rho$	$\rightarrow 1$	IRBis
$\mathrm{q_{rec}}$	$\rightarrow 0$	IRBis

Table 3.1.: Quality parameters for image reconstruction

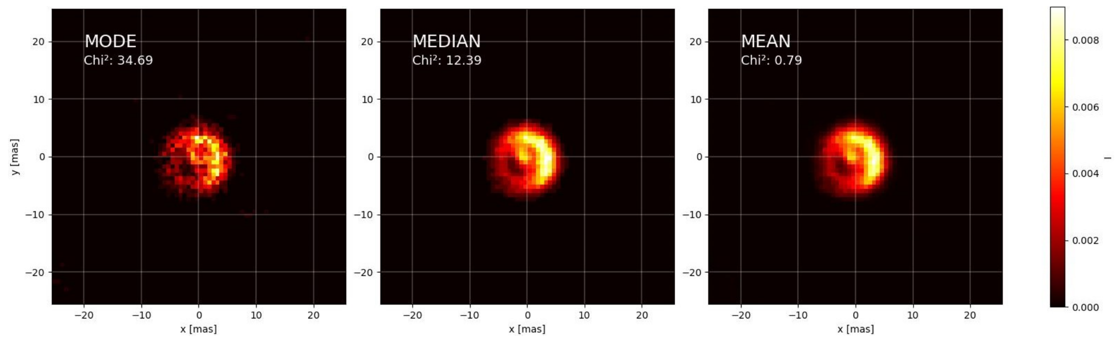

Figure 3.2.: First reconstruction of LkHa101 (image-beauty-contest 2004 dataset1) with SQUEEZE, showing the three different outputs: MODE (*top left*), MEDIAN (*top right*) and MEAN (*bottom left*).

3.4. Methods used

Three image reconstruction tools: SQUEEZE, MiRA and IRBis were used in this work and are described in the following sections.

3.4.1. SQUEEZE

SQUEEZE, developed by Fabien Baron and John Monnier ([BMK10]), is a multispectral tool for image reconstruction for optical/IR interferometric data. To find the best image, that fits the data a MCMC algorithm is applied. Therefore, measurements of Visibilities, Powerspectra, Bispectra or combinations of them can be used.

The software and its documentation can be downloaded at: `https://github.com/fabienbaron/squeeze`. For detailed information see [BMK10].

SQUEEZE provides for each reconstruction run three different results: the MODE, the MEDIAN and the MEAN (see Figure 3.2). The one that represents the image best is the MEAN. Compared to the MEAN, the MODE will give a more discretized image and the MEDIAN a more spread one. This conclusion is based on reconstruction tests with the image-beauty-contest 2004 ([LCH+04]) data[2], LkHa101, and on the results of various scientific papers. ([TY17], [STD+16])

SQUEEZE offers a variety of different regularization functions (see [STD+16]). Those used in this work (total variation (-tv), uniform-disk (-ud) and l0-sparsity norm (l0), see Figure 3.3) were obtained by reconstruction tests and selected by the lowest χ^2-values.

The total variation (-tv) helps to describe uniform areas with steep, but localised changes and hence conserves important details (e.g. sharp edges). However, it produces cartoon-like artifacts. ([RTM11], [TY17])

The uniform disk regularization function (-ud) prevents the pixels from approaching a value of zero and hence enforces positivity ([TY17], [STD+16])

[2]available at `https://github.com/fabienbaron/squeeze/tree/master/sample_data`

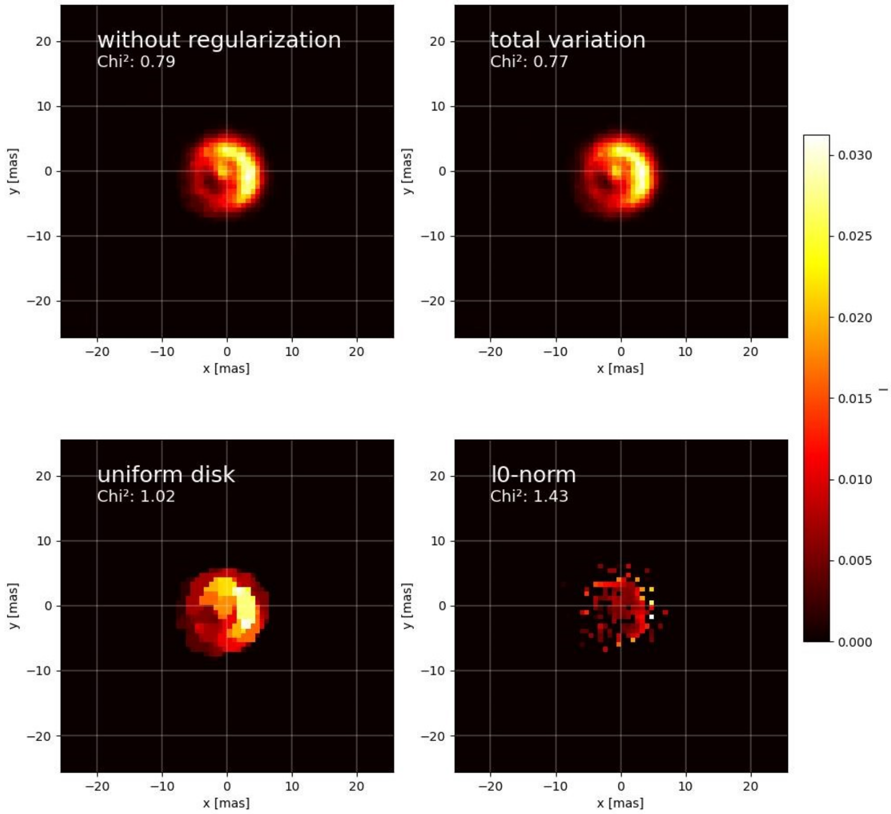

Figure 3.3.: LkHa101 reconstructed with SQUEEZE, attempting different regularization functions (regularization parameter $\mu = 10$).

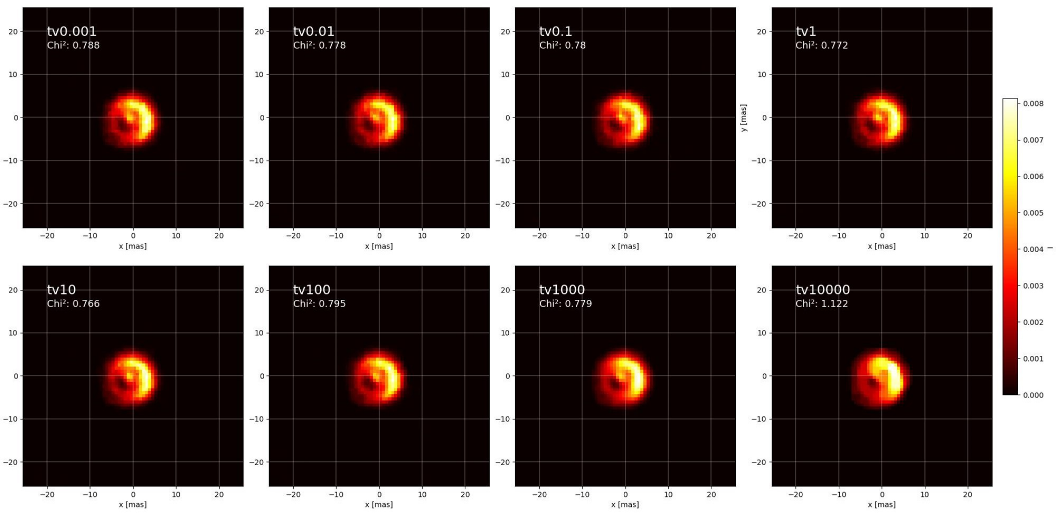

Figure 3.4.: LkHa101 reconstructed with SQUEEZE and the total variation regularization function, attempting different regularization parameters μ.

The l0-sparsity norm will force the image to be the sparsest solution, therefore enforces many parameters to be zero. ([STD$^+$16] ,[TY17])

The hyperparameter μ, that has to be chosen to hold the correct balance between the data and the priors can be determined by visual inspections (see Figure 3.4)([TY17]).

Additionally, a starting image can be implemented, either by using a pre-existing image (-i), or by using a random pixelset (-random).

3.4.2. MiRA

The **M**ulti-aperture **I**mage **R**econstruction **A**lgorithm, called MiRA, developed by Éric Thiébaut ([Thi08]), tries to find an image that fits best to the data and a pre-defined model (see Equation 3.1). Therefore, it uses an adapted gradient-based method. It can handle any interferometric data, including complex visibilities, powerspectra or closure phases.

The software can be used stand-alone, or as in this work, via the OImaging-tool from JMMC. ([Thi21], [STD$^+$16])

MiRA offers two different regularization functions (quadratic compactness and edge-preserving smoothness, see Figure 3.5):

The quadratic compactness assumes a gaussian prior, as well as positivity. The emerging artefacts are formed as ripples around sharp structures ([TY17]).

The edge-preserving smoothness (inside MiRa called "hyperbolic") conserves sharp structures, while restraining the cartoon-like artefacts of the total variation employed by SQUEEZE. It is parameterized by the edge treshold τ (see Figure 3.6) and the scale η. If τ is very small this regularization function acts like the total variation, while if τ takes large values it is comparable to the quadratic smoothness function. η roughly estimates the local gradient. Its default is set to 1. The parameter REG_WGT weights between the data and the regularizations (see Figure 3.7). ([Thi21],[STD$^+$16])

Unlike SQUEEZE, MiRA requires a starting image. This can either be uploaded or generated directly in OImager using a Gauss-function.

3.4.3. IRBis

The **I**mage **R**econstruction software using the **Bis**pectrum, short IRBis, was developed by K.H. Hofmann ([HWS14]). It uses a large-scale (number of pixels in the reconstructed image $\sim 10^4 - 10^5$), bound-constrained, gradient minimization routine. IRBis calculates different reconstructions with different values for a circular image mask and the regularization parameter, μ, and decides on the 'best' image using different quality-criteria parameters. Furthermore, each image mask radius run contains various regularization parameter runs that vary the regularization parameter. As the starting value for the next run either the priors, or the best estimate from the previous run, or the best reconstruction from all previous runs can be utilized. A varied range of experiments shows that using the image reconstructed in the previous run is the best approach in order to converge to a plausible result as quickly as possible. ([HWS14])

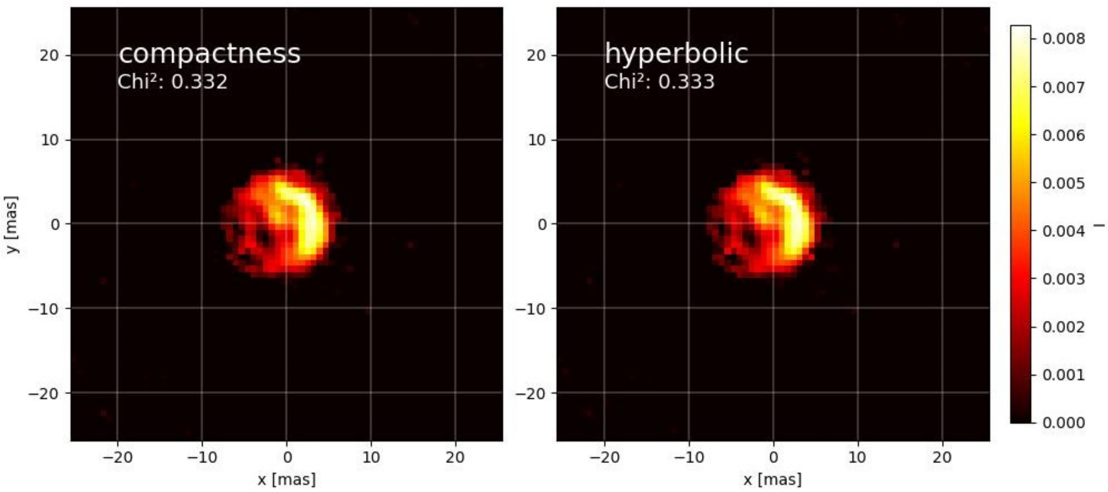

Figure 3.5.: LkHa101 reconstructed with MiRa, comparing the two different regularization functions. *left:* quadratic compactness, *right:* edge-preserving smootness (inside MiRa called "hyperbolic")

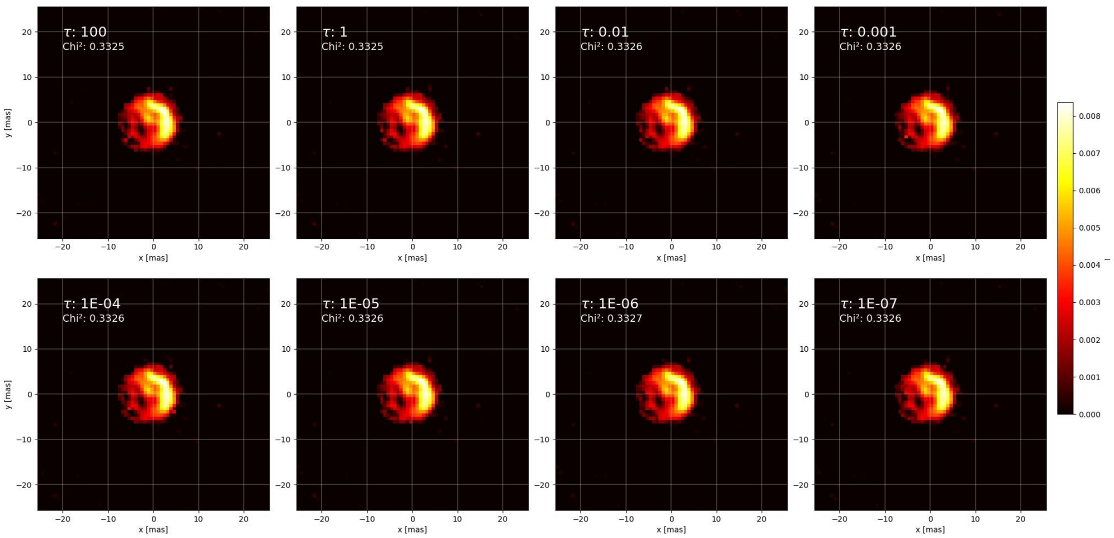

Figure 3.6.: LkHa101 reconstructed with MiRa, attempting different regularization parameters τ.

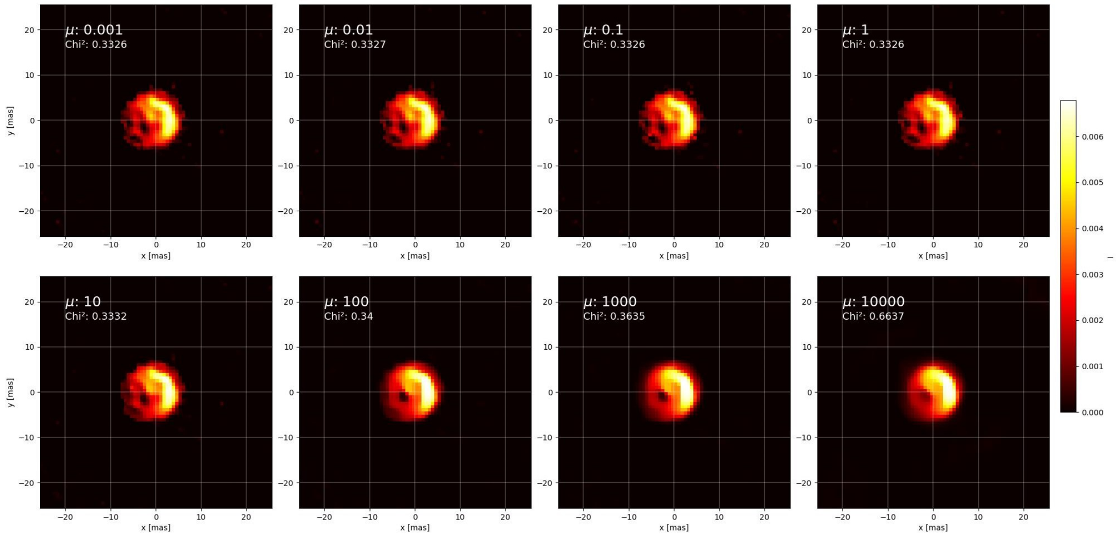

Figure 3.7.: LkHa101 reconstructed with MiRa, attempting different regularization weights RGL_WGT that represents the hyperparameter μ.

IRBis contains a large variety of different regularization functions, including maximum entropy, edge preserving and smoothness, to name here just a few of them. Additionally, all of these functions can be marked by a negative sign, which implies, that no estimate of the target is done, hence the prior image is set to a constant value. A comparison of the regularization functions (without starting image) is plotted in Figure 3.8, while the hyperparameter μ is varied in Figure 3.9. ([HWS14])

The used starting image can either be a pre-existing one or chosen out of the following provided start image functions: point source, Gaussian, Uniform disk, Fully darkend disk, Lorentzian function.

Before starting an image reconstruction run, IRBis offers the possibility to perform a parameter estimation run. These values can then be used to start the image reconstruction run. The most important ones are listed in Table 3.2.

Additionally, a graph with the fitted models (see Figure 3.10) and the uv-plane (see Figure 3.11) are provided by the IRBis software.

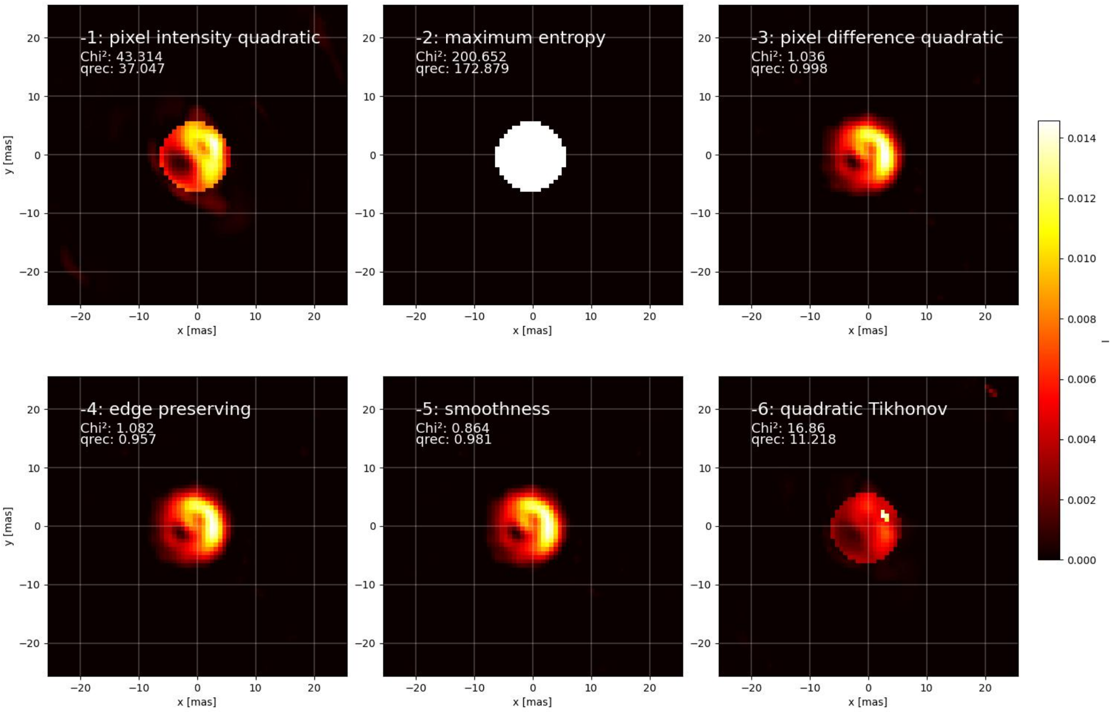

Figure 3.8.: LkHa101 reconstructed with IRBis, attempting different regularization functions.

parameter	value
(A) Information about the data:	
$\lambda_{\min}$ [m]	5.5×10^{-7}
$\lambda_{\max}$ [m]	5.5×10^{-7}
(B) Estimated target size by fitting the V^2 data:	
(2) Gaussian FWHM [mas] (red. Chi^2)	4.505 (1337.064)
(3) Uniform disk diameter [mas] (red. Chi^2)	6.739 (570.013)
(4) Fully darkened disk diameter [mas] (red. Chi^2)	7.61 (716.594)
(C) Recommended size of angular FOV & size of NxN pixel grid:	
FOV (64x64 pixels) [mas]	27.346
FOV (128x128 pixels) [mas]	54.691

Table 3.2.: Values of the most important estimated parameters during the parameter estimation run of IRBis, that are listed in the file 'data.parameter' for the LkHa data.

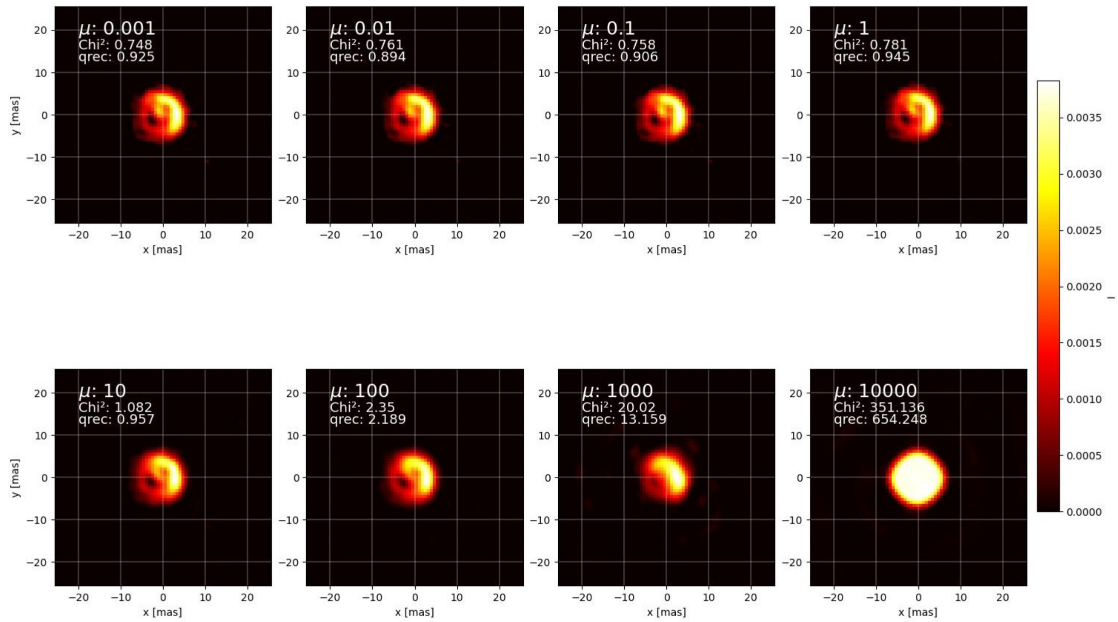

Figure 3.9.: LkHa101 reconstructed with IRBis, using the 'pixel difference quadratic' regularization function (-3), attempting different regularization parameters μ.

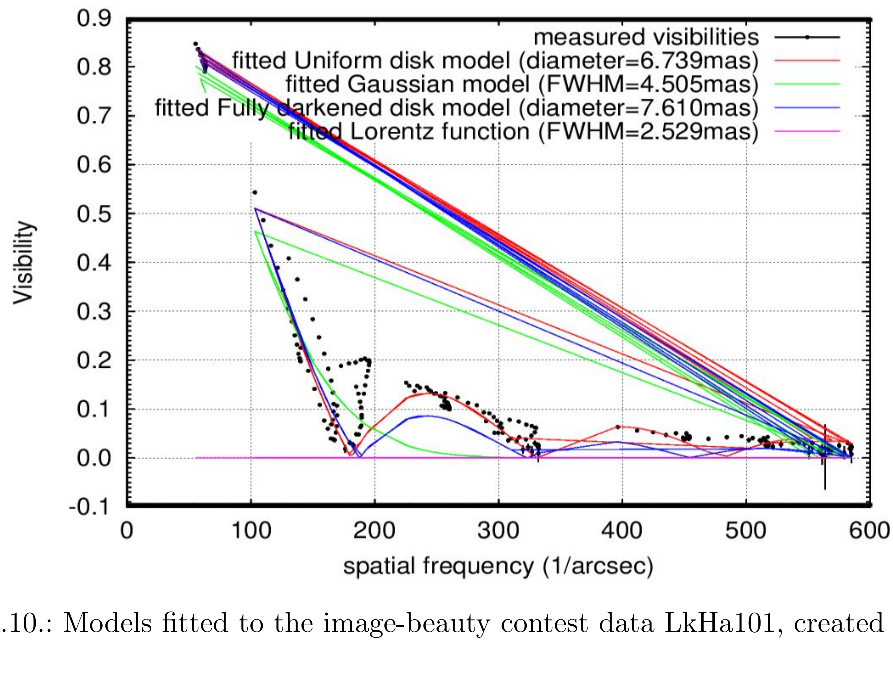

Figure 3.10.: Models fitted to the image-beauty contest data LkHa101, created by IRBis

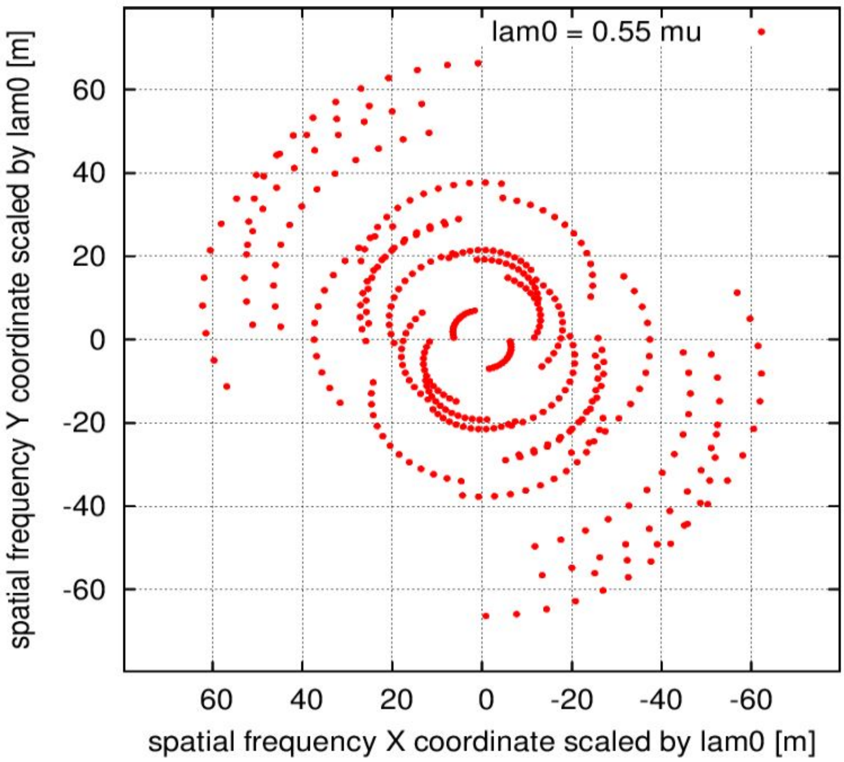

Figure 3.11.: The uv-plane of the image-beauty contest data LkHa101, provided by IRBis

4. DATA

4.1. R Sculptoris data

As mentioned previously, the object studied in this work is R Sculptors and the data used in this work was obtained during the comissioning phase of MATISSE in December 2018. Containing squared visibilities (VIS2) and closure phases (T3), the data are visualized in the following Figures by using the JMMC tool *OIFitsExplorer*[1]. The data quality was assessed before starting the image reconstruction process, according to the criteria listed in Table 4.1. All the data is presented in Figure 4.1.

data quality	available BCDs	V2	closure phases	tracking ratios (TR)
good	all	OK	OK	min. 3 TR > 0.5
medium	some missing	strange	strange	min. 2 TR ≤ 0.5

Table 4.1.: Quality criteria for the R Sculptoris data. For the good data, all parameters must fit the quality criteria, while for the medium data just one or more of these (bad) quality criteria must be fulfilled.

After the quality check the BCDs were merged using *mattools*, a tool provided by the MATISSE consortium[2]. The merged data are shown in Figure 4.2.

4.1.1. Data processing

To reconstruct images in individual wavelength ranges, the associated data has to be extracted.

Therefore, the data is split into wavelength channels/bins (see Figure 4.3 and 1.7) to focus on specific molecular features in the stellar atmosphere and close environment. Following an earlier work of Hron et al. ([HLH+98]), the assignment to the individual spectral features was made by Drevon et al. ([DMC+22]). The prominent features in the LM-band around 3.1 μm and 3.52 μm (C_2H_2, HCN, C_2) show the biggest changes in morphology, hence they were used for further investigation by image reconstruction.

The visibility plots in each wavelength bin are shown in Figure 4.4.

Figure 4.5 plots the uv-planes of the obtained data.

[1] available at `https://www.jmmc.fr/english/tools/data-analysis/oifits-explorer/`

[2] available at https://gitlab.oca.eu/MATISSE/tools

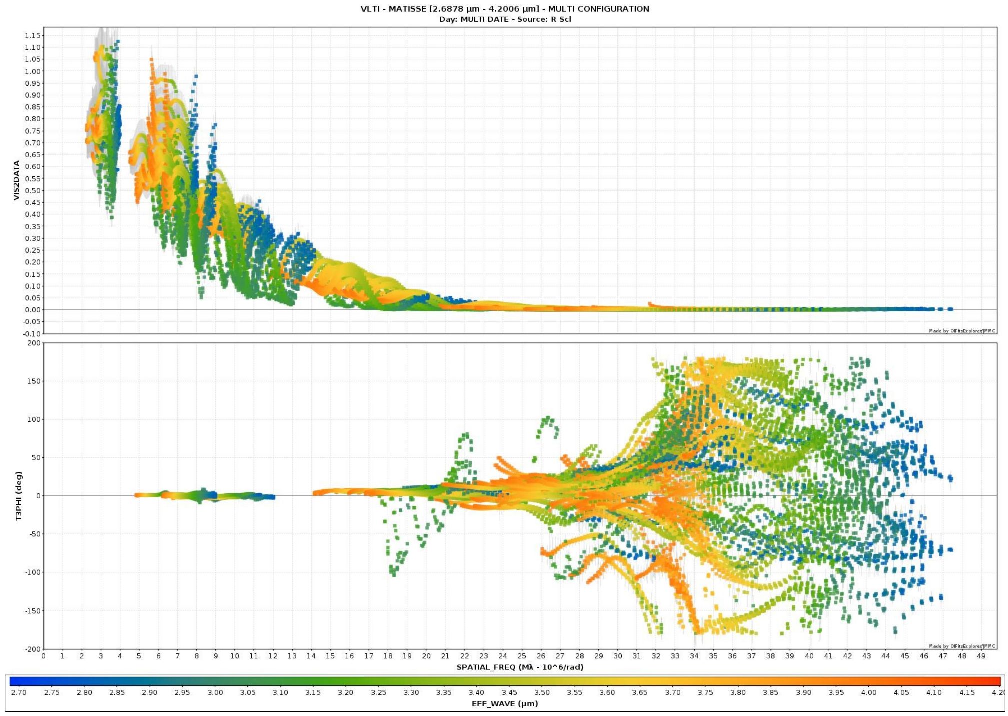

(a)

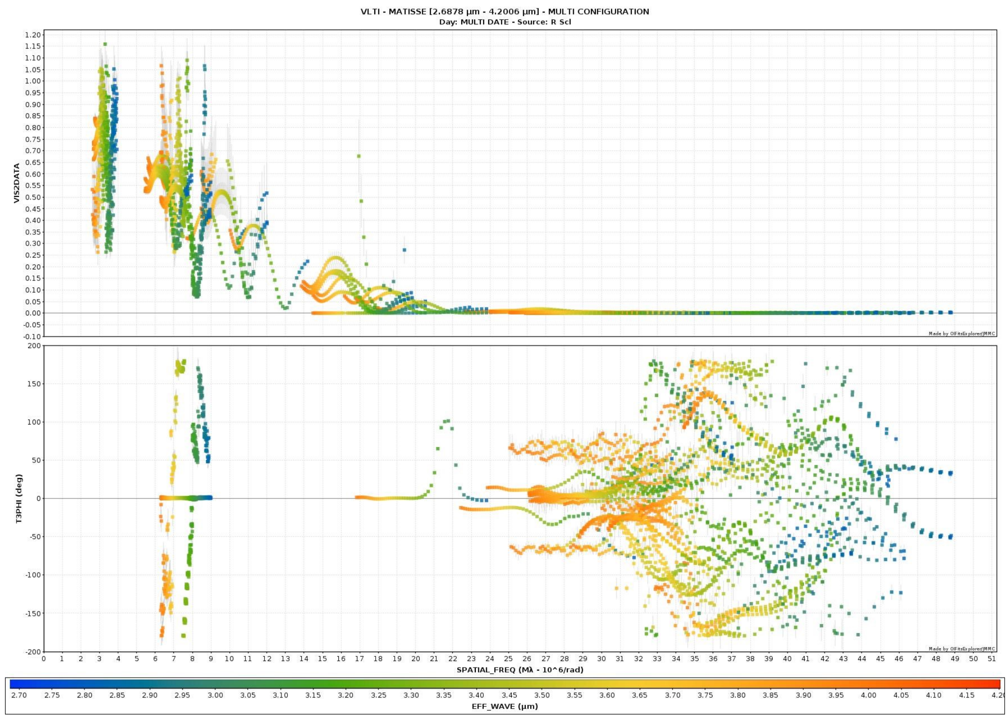

(b)

Figure 4.1.: R Sculptoris data in the LM-band for the different quality characteristics: a) good data, b) medium data. *top panels:* squared visibilities (VIS2), *bottom panels:* closure phases (T3PHI)

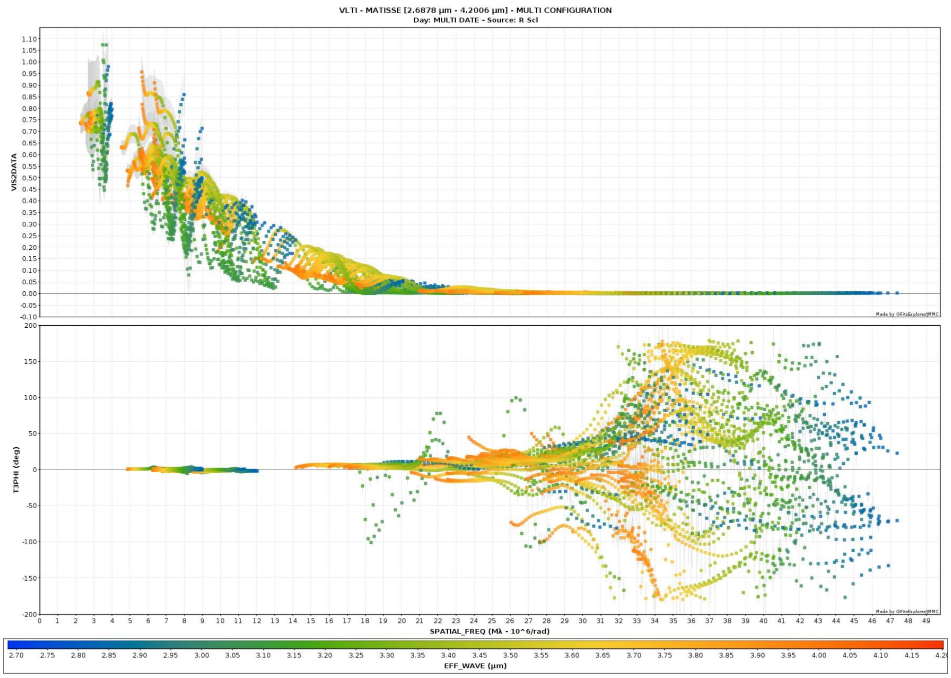

Figure 4.2.: BCD-merged, good R Scl data

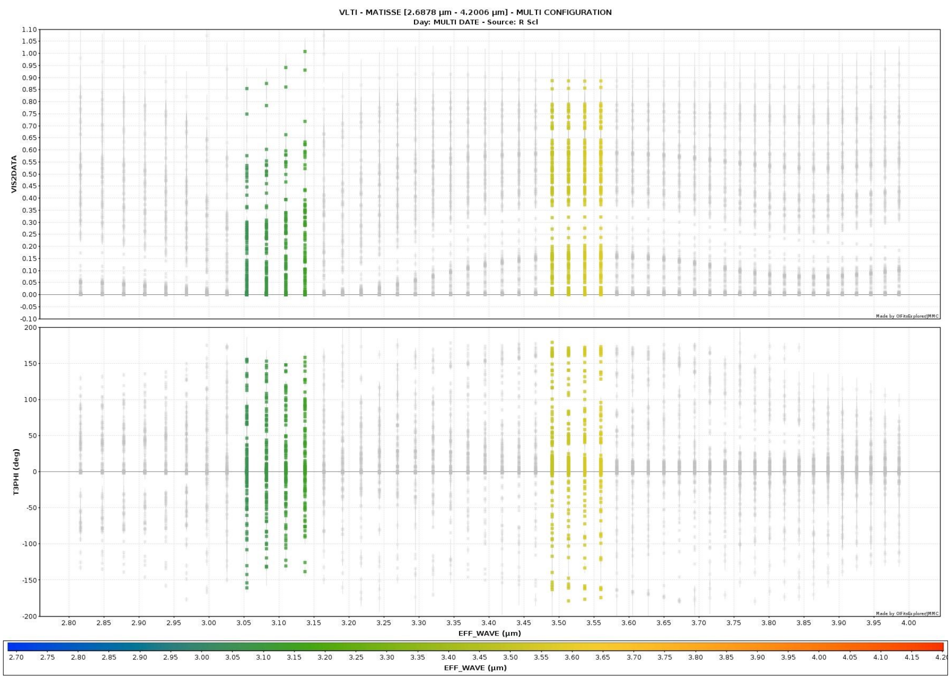

Figure 4.3.: Defined wavelength-ranges and set filters for the BCD-merged R Scl data in the L- and M-band. *green:* 3.05 μm $\leq \lambda \leq$ 3.15 μm, *yellow:* 3.47 μm $\leq \lambda \leq$ 3.57 μm, *grey:* not selected

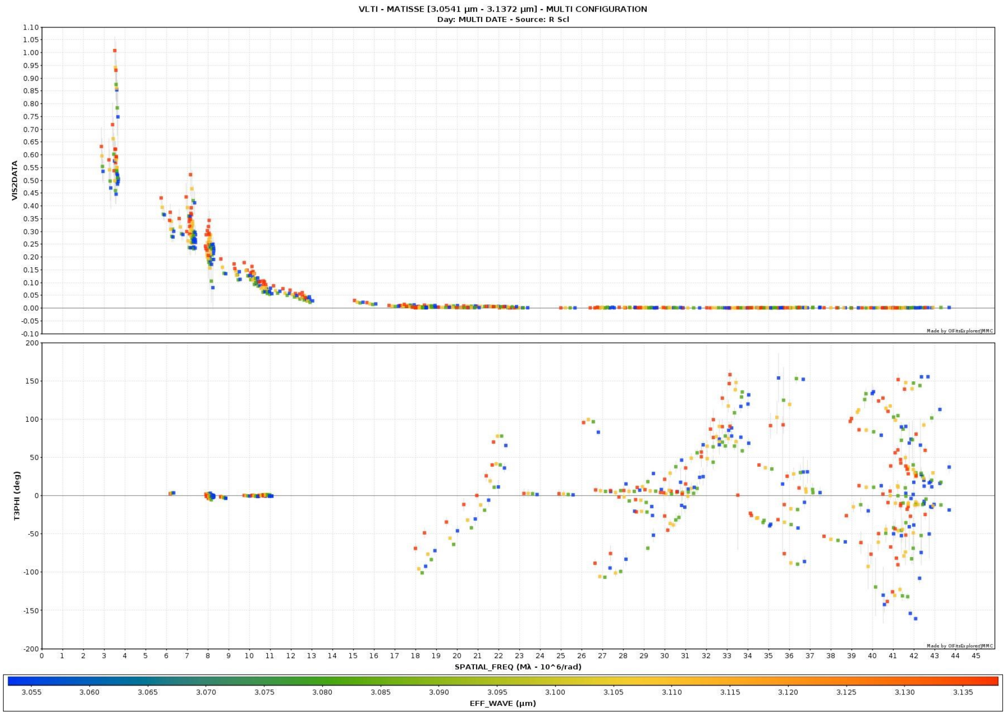

(a)

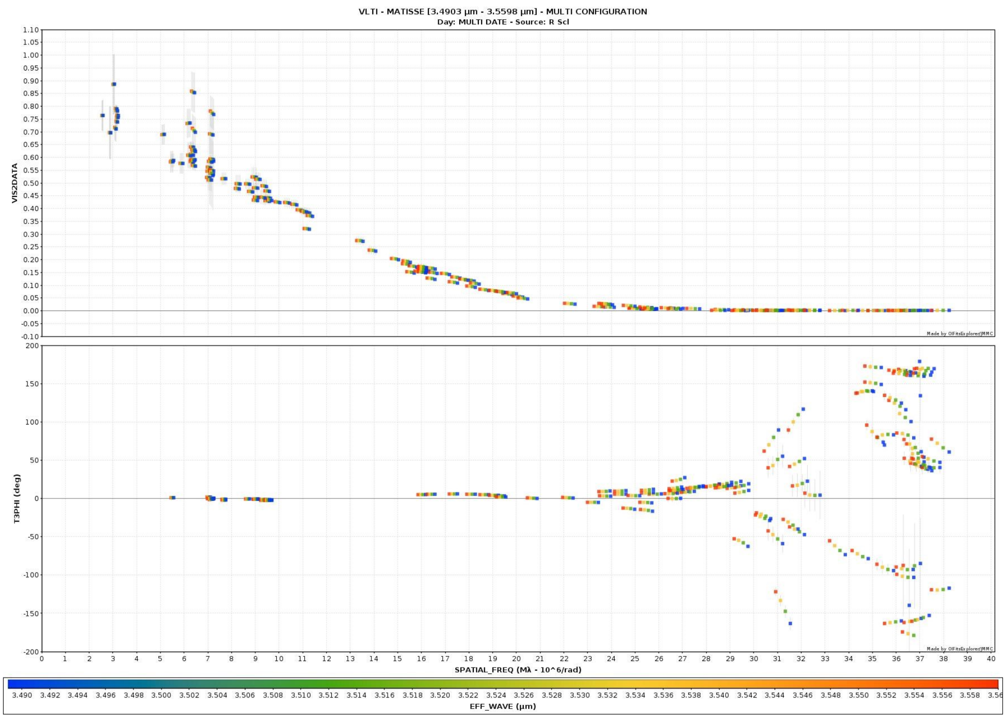

(b)

Figure 4.4.: Individual BCD-merged R Scl data for the a) 3.1 μm and b) 3.52 μm wavelength ranges

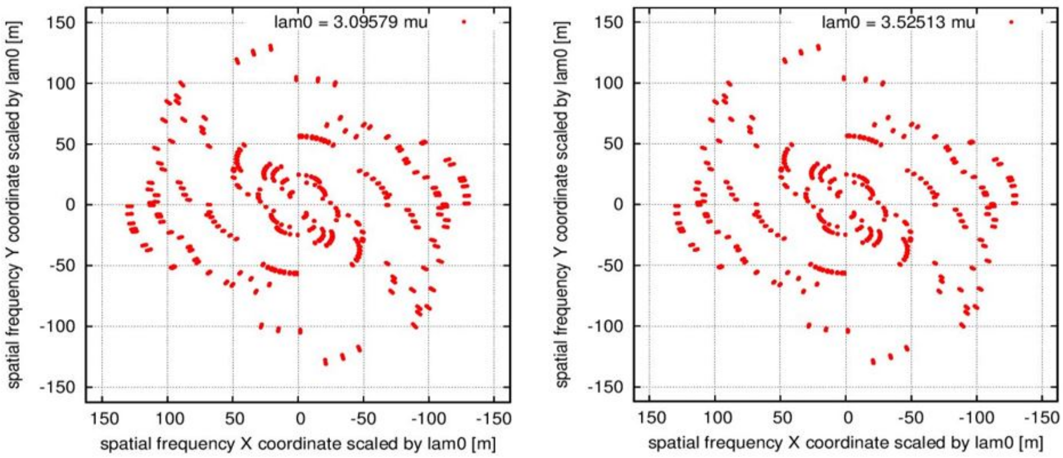

Figure 4.5.: The uv-plane of the BCD-merged R Scl data, obtained by MATISSE. *left:* 3.1 μm data, *right:* 3.52 μm data

5. RESULTS

5.1. LkHa 101

For the first tests synthetic data created for the image beauty contest 2004 ([LCH+04]) were used[1]. Based on this data, tests on the different regularization functions and hyperparameters μ are done for all three image reconstruction tools (see Section 3.4).

A comparison between the best reconstructed images of these three tools is shown in Figure 5.1.

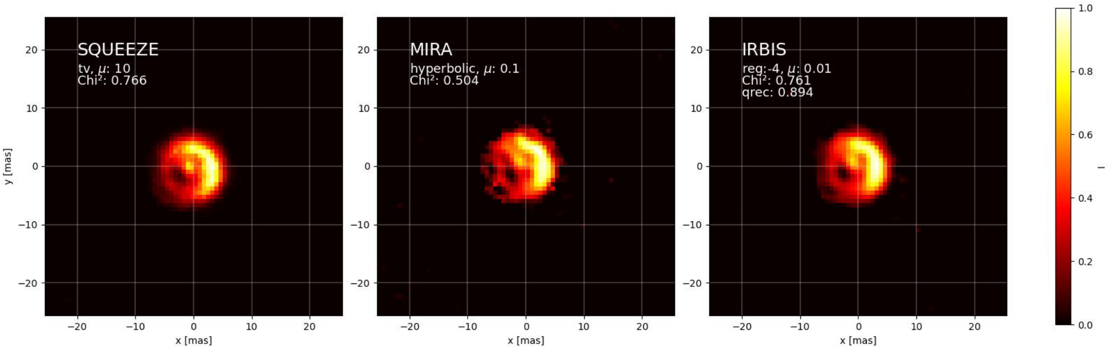

Figure 5.1.: LkHa101 reconstructed with SQUEEZE (*left*), MiRA (*middle*) and IRBis (*right*) with the each best parameters.

5.2. R Scl data

Image reconstruction was accomplished for BCD-merged and -unmerged data of R Scl (see Chapter 4). Therefore, a variety of different parameter settings were tested for the different reconstruction methods. The best reconstructed images are selected with respect to the quality parameters χ^2 and q_{rec} (see Section 3.3) and visual inspections. As reference the result of Drevon et al. ([DMC+22]), obtained with MiRA, is used.

5.2.1. 3.1 μm

Figure 5.2 shows the best reconstructed images for the wavelength range 3.1 μm, resulting from the unmerged data. In the top-left panel the result from Drevon et al. ([DMC+22]) is plotted. The other panels show different reconstruction runs with SQUEEZE, using the

[1] available at `https://github.com/fabienbaron/squeeze/tree/master/sample_data`

same pixel size s (obtained by Equation 5.1), number of interrations n and regularization function, but varying the regularization parameter μ. Total variation was used as the regularization function, since reconstruction tests showed most promising results using this method. The number of interrations was not increased further since no significant change was recognizable by changing it.

$$s \leq \frac{\lambda}{4 \cdot \mathrm{B_{max}}} \tag{5.1}$$

It is clearly visible that the objects reconstructed by SQUEEZE are bigger in size, grainier, have a less clear structure and have more background noise than the images obtained by Drevon et al. [DMC+22]. Smoothing the images would be a possibility to clear the grainy aspect of the structure, but might lead to the loss of visible structure. Hence, no smoothing was done as part of this work. The higher amount of background noise could be due to the different reconstruction algorithms or due to the slight differences in the selection of the dataset.

Intensity profiles were created for the purpose of analysing the images, following the approach of Drevon et al. ([DMC+22]) (see Figure 5.3). In their image a significant bump is seen along the x-axis on the left side, marking the transition between the shell-like structure and the central bright spot. A similar transition can be observed on the right side, although not as pronounced. These structures can be recognised in the SQUEEZE reconstructions done as part of this work, especially in A113 (see Figure 5.3, lower left panel).

The profile generated by a cut along the y-axis from the Drevon study is also reproduced quite well. The profiles are in accordance with the images, showing the emission peak in the north-west quadrant.

Additionally, the larger extension of the object is represented as wider structure of the horizontal and vertical slice-plots.

Figure 5.4 displays the best reconstructions from the three different reconstruction tools (SQUEEZE, MiRa and IRBis) when using the BCD-merged data of R Scl, showing much more consistent results, while their parameters are summarized in Table 5.1.

The horizontal and vertical profiles (see Figure 5.5) are much smoother when using the merged-BCD data. Overall, the reconstruction methods were able to reproduce the maximum peak as well as its slightly decentered peak-position. Additionally the bump in the horizontal cuts (blue lines), that marks the border of the outer fainter environment, is more or less prominant in all images. The shell structure on the lower part of the object, which can be seen as a bump on the right (approximately at y = 65 px) in the vertical cuts (red lines), is reproduced quite well by the IRBis algorithm, while with SQUEEZE a small second peak is visible — probably due to the grainy structure of the reconstructed image. The resulting MiRa image only shows a very faint feature in the profiles.

Additionally, the width of the profiles show that the whole structure (bright center and faint shell environment) are reconstructed to a similar size with all algorithms. However, the horizontal plots (blue) have a slimmer peak (smaller FWHM), highlighting the elongated structure of the images.

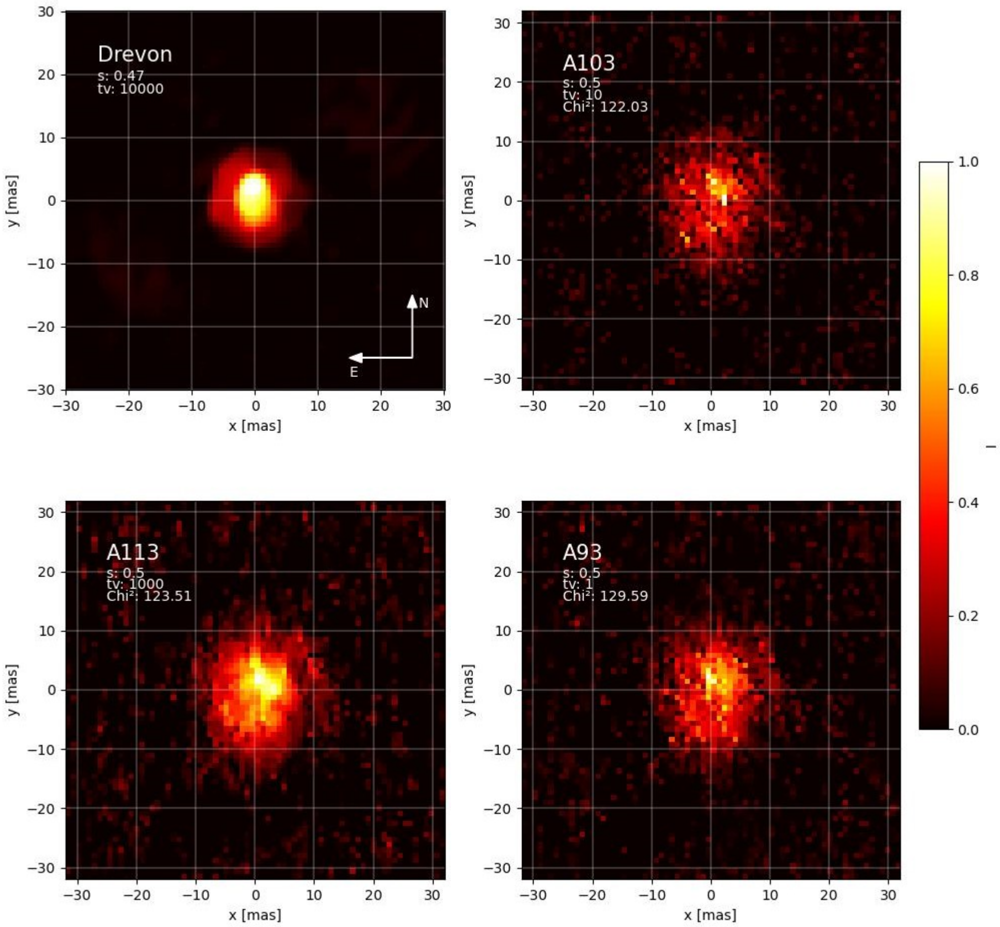

Figure 5.2.: Reconstructions of R Scl 3.1 μm, not-merged data with SQUEEZE by varying the regularization parameter μ, compared to the work of Drevon et al. [DMC+22] (*top left*). North is up, East is left (this applies to all subsequent images)

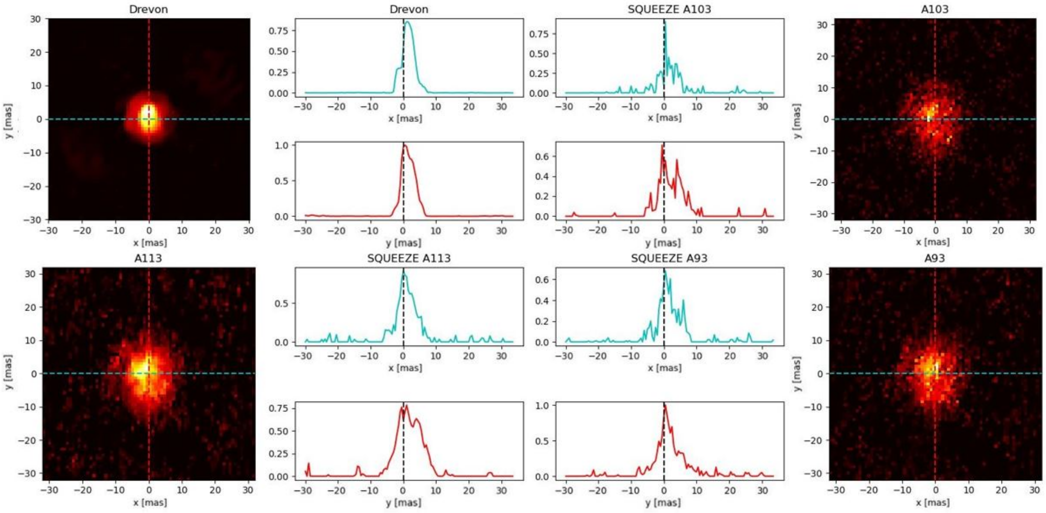

Figure 5.3.: R Scl 3.1 μm not-merged intensity profiles *blue:* horizontal, *red:* vertical, *dotted:* cut-line for intensity profiles horizontal and vertical respectively.

Radial profiles of the images were also computed, by splitting the plots in twelve 30 degree sections. The starting point of the profiles is the gravitational center and the pixel intensities are scaled with respect to the central pixel (which is set to have an intensity of one). Figure 5.6 summarizes the radial profiles and the chosen sections for the images reconstructed with SQUEEZE. The blue circle marks a 50 pixel radial distance and encompasses the entire structure seen in the images. The radial profiles show no structures in the outer regions.

The error of the profiles is shown as a light-blue region around the curves and it signifies a 1-sigma deviation (STDV).

A comparison of radial profiles obtained for each reconstruction method and the results of Drevon et al. ([DMC+22]) can be seen in Figure 5.7, covering only 30 mas from the center.

The overall shape of the reconstructions are similar to each other. The radial profiles of the SQUEEZE data (yellow lines) show, unlike the other methods, a steep increase in intensity in the central regions. Especially in the upper right regions (270°–360°), which leads to the assumption that the central bright structure might be shifted from the center of gravity. This result is supported by the fact that all images, regardless of the method employed in obtaining them, show this intensity shift towards the north-western quadrant (see Figure 5.4).

The bump marking the shell-border is clearly visible in the radial profiles in a region between 30 and 120 degrees and is reconstructed by the different algorithms.

Based on this, the shell spans a region between 5 and 12 mas.

Additional radial profile plots, containing the STDV are stored in the Appendix (see Appendix A.1).

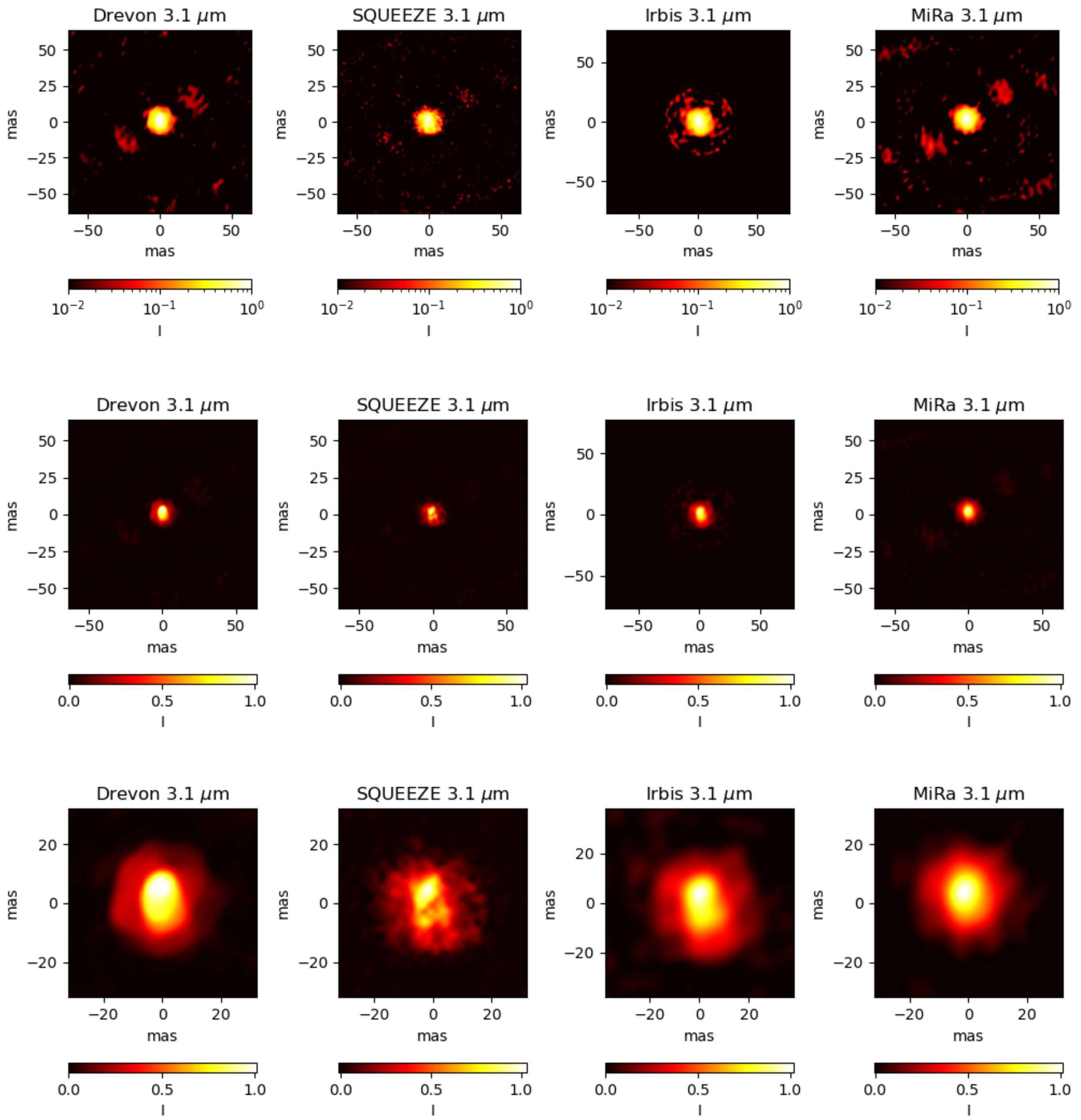

Figure 5.4.: Comparison of the reconstructed images with SQUEEZE, MiRa and IRBis of R Scl at 3.1 μm (BCD-merged data) and the result obtained by Drevon et al. ([DMC+22]). *top:* original size logarithmic scale, *middle:* original size linear scale, *bottom:* zoom into the central part linear scale

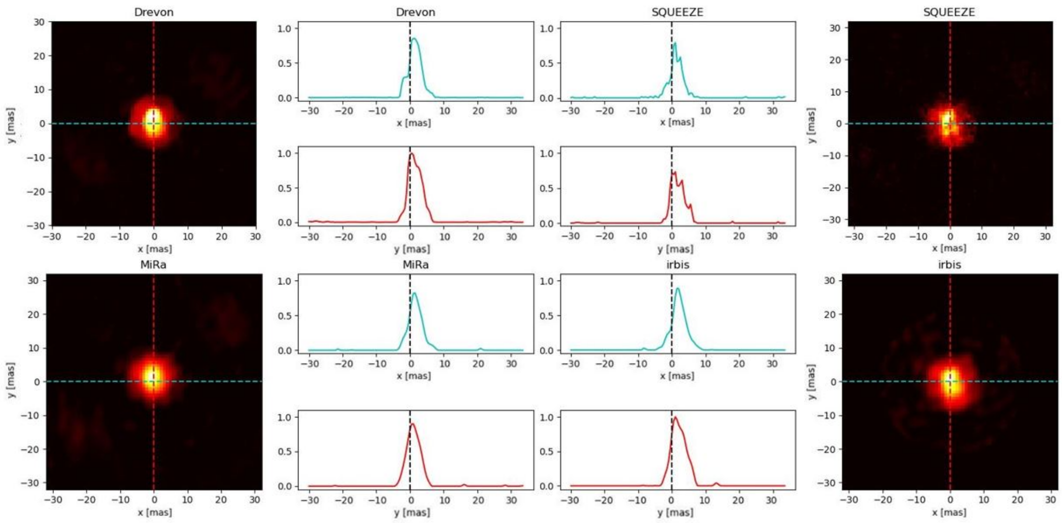

Figure 5.5.: R Scl 3.1 μm BCD-megered intensity profiles *blue:* horizontal, *red:* vertical, *dotted:* cut-line for intensity profiles horizontal and vertical respectively.

5.2.2. 3.52 μm

The same analysis was done with the observations of R Scl at 3.52 μm. Figure 5.8 summarizes the best reconstructed images of the different algorithms and Table 5.1 contains their parameters. It is clearly visible that the structure is not as prominent as at 3.1 μm. Despite it, a slightly triangular shape, surrounded by a shell that is more extended in the vertical direction, is present in all the reconstructed images.

To verify this, horizontal and vertical intensity (see Figure 5.9) and radial profiles (Figure 5.10 and 5.11) were plotted.

Figure 5.9 does not show broad bumps, inferring that the shell structure is relatively thin. The image produced by Drevon et al. ([DMC+22]) and the one reconstructed with IRBis show a faint bump in the horizontal intensity cut.

In comparison to the images obtained at 3.1 μm the radial profiles (see Figure 5.11), as well as the images itself, infer the presence of a thinner shell, but at the same time the central source is bigger and more pronounced.

5.3. Artefacts

In order to determine if the obtained structures are real or artefacts, different methods can be used.

One such method is using different reconstruction algorithms, the result of which is summarized above. Another way is to calculate synthetic observational data from the reconstructed image and use this as input for a new reconstruction. For this purpose,

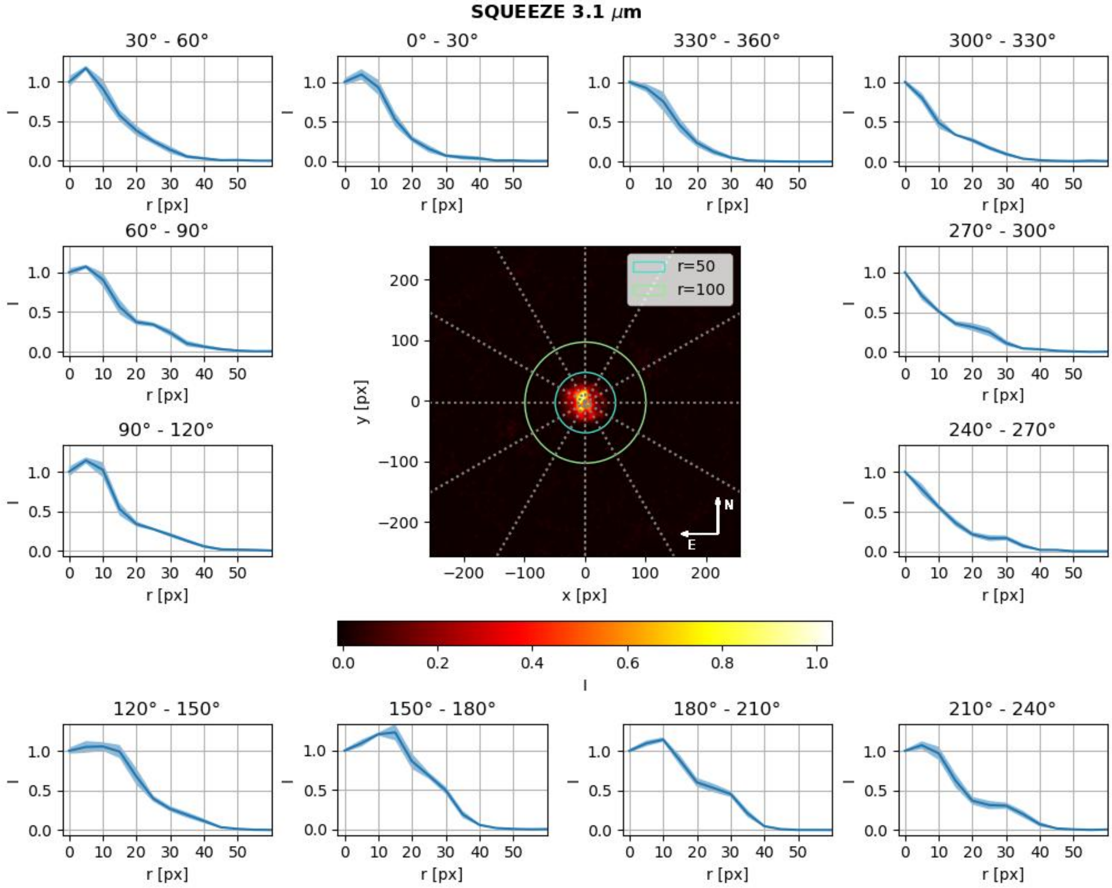

Figure 5.6.: R Scl 3.1 μm merged radial profiles SQUEEZE

3.1 μm

algorithm	χ^2	q_{rec}	reg. fct.	μ	starting image
SQUEEZE	2.995	-	tv	10	-
MiRa	0.55	-	hyperbolic	0.001	FWHM=10mas
IRBis	4.116	1.571	pixel difference quadratic (-3)	1000x0.001 n=3	Gauss (2), FWHM=10mas

3.52 μm

algorithm	χ^2	q_{rec}	reg. fct.	μ	starting image
SQUEEZE	1.605	-	tv	10	-
MiRa	0.383	-	hyperbolic	0.001	FWHM=7mas
IRBis	14.446	7.601	quadratic Tikhonov (-6)	1000x0.001 n=3	Gauss (2), FWHM=10mas

Table 5.1.: Quality parameters of the reconstructed images of R Scl in 3.1 μm and 3.52 μm with the different used image reconstruction algoithms.

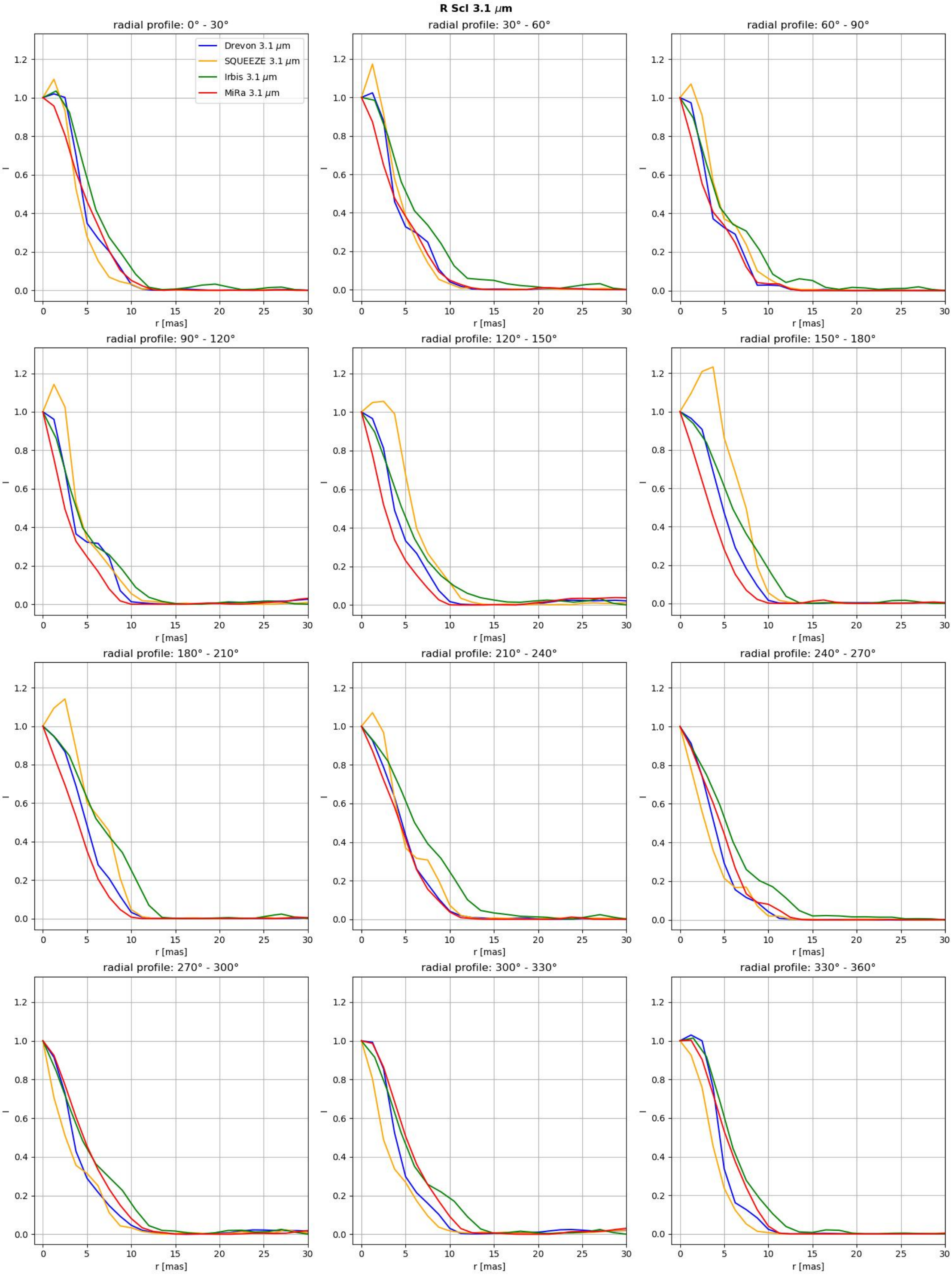

Figure 5.7.: R Scl 3.1 μm merged radial profiles ALL

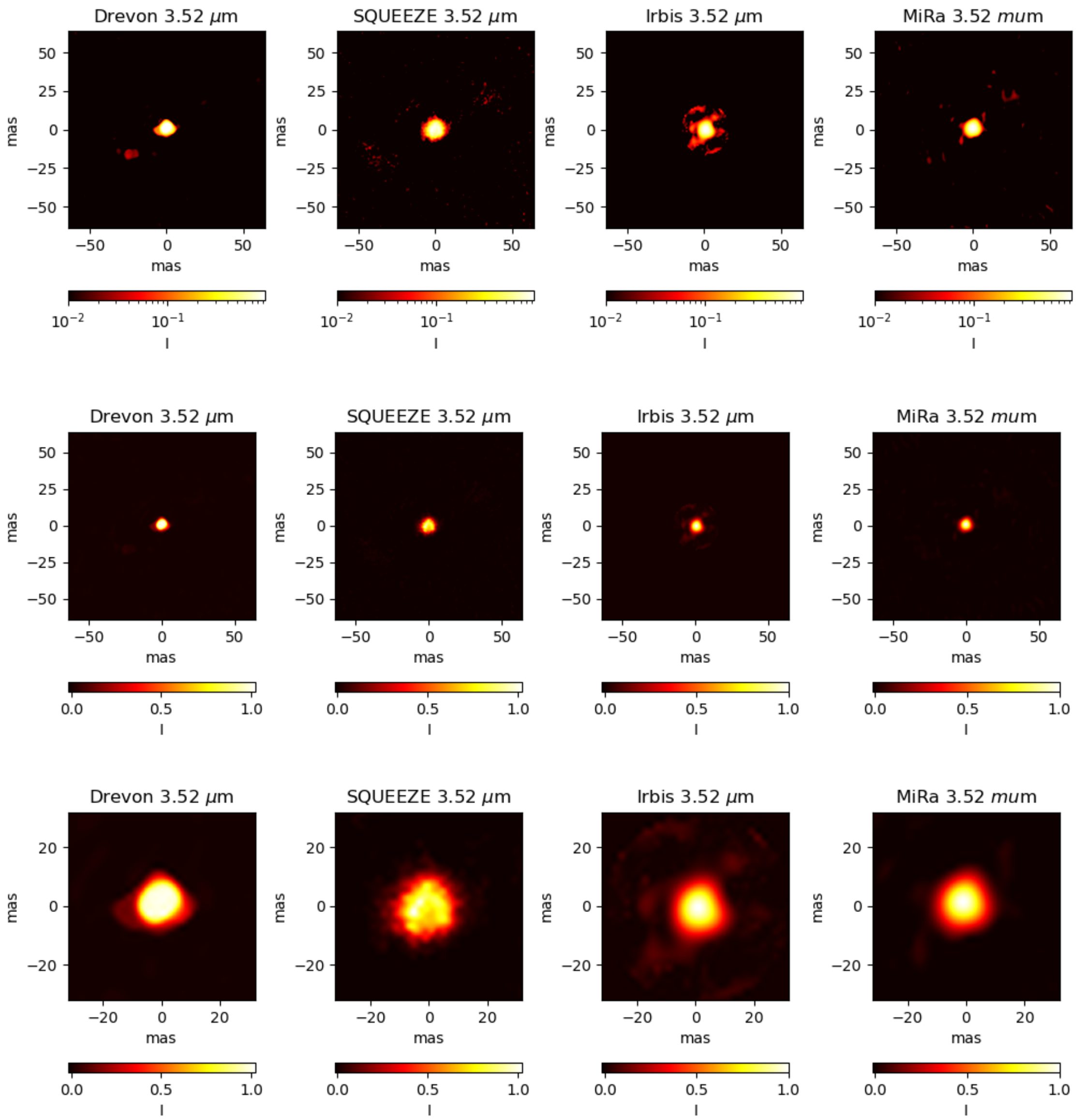

Figure 5.8.: Comparison of the reconstructed images with SQUEEZE, MiRa and IRBis of R Scl at 3.52 μm (BCD-merged data) and the result obtained by Drevon et al. ([DMC+22]). *top:* original size, logarithmic scale, *middle:* original size, linear scale, *bottom:* zoom into the central part, linear scale

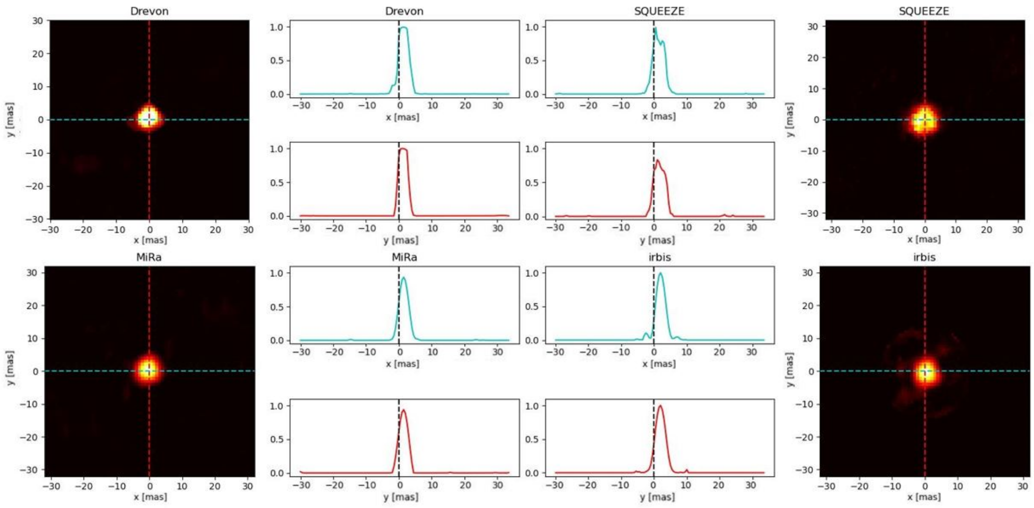

Figure 5.9.: R Scl 3.52 μm BCD-megered intensity profiles *blue:* horizontal, *red:* vertical, *dotted:* cut-line for intensity profiles horizontal and vertical respectively.

the online-software tool AMHRA OIfits-modeler[2], that calculates synthetic observational data from an input image was used. This method was applied in three different ways:

1. The reconstructed image was used as input for AMHRA, this way testing the reproducibility of the reconstruction (see Figure 5.12 and 5.13).
2. The reconstructed image was flipped 180 degrees vertically before beeing used as input, to identify artefacts due to the reconstruction process (see Figure 5.14 and 5.15).
3. Since the initial result shows an elongation along the vertical axis, the images were also rotated by 90 degrees (counter-clockwise) in order to more accurately determine what features are artefacts and which ones can be considered real. (see Figure 5.17 and 5.18).

In all three cases the synthetic interferometric data were extracted from the input images by using the same (u,v)-coverage, the same error-values and the same quality flags as the original observational data. Further, the re-reconstructions were calculated by using the same reconstruction method as for the AMHRA-input files and using the same parameters as in the initial run. ([PPJ+24])

Figure 5.12 and 5.13 show the re-reconstructions with the upright images used as AMHRA-input. The upper rows in each Figure show the input files that were used to generate the synthetic observations, while the lower panels show the re-reconstructed images, both are also plotted in a logarithmic scale. It is clearly visible that the overall

[2] https://amhra.oca.eu/AMHRA/oifits-modeler/input.htm

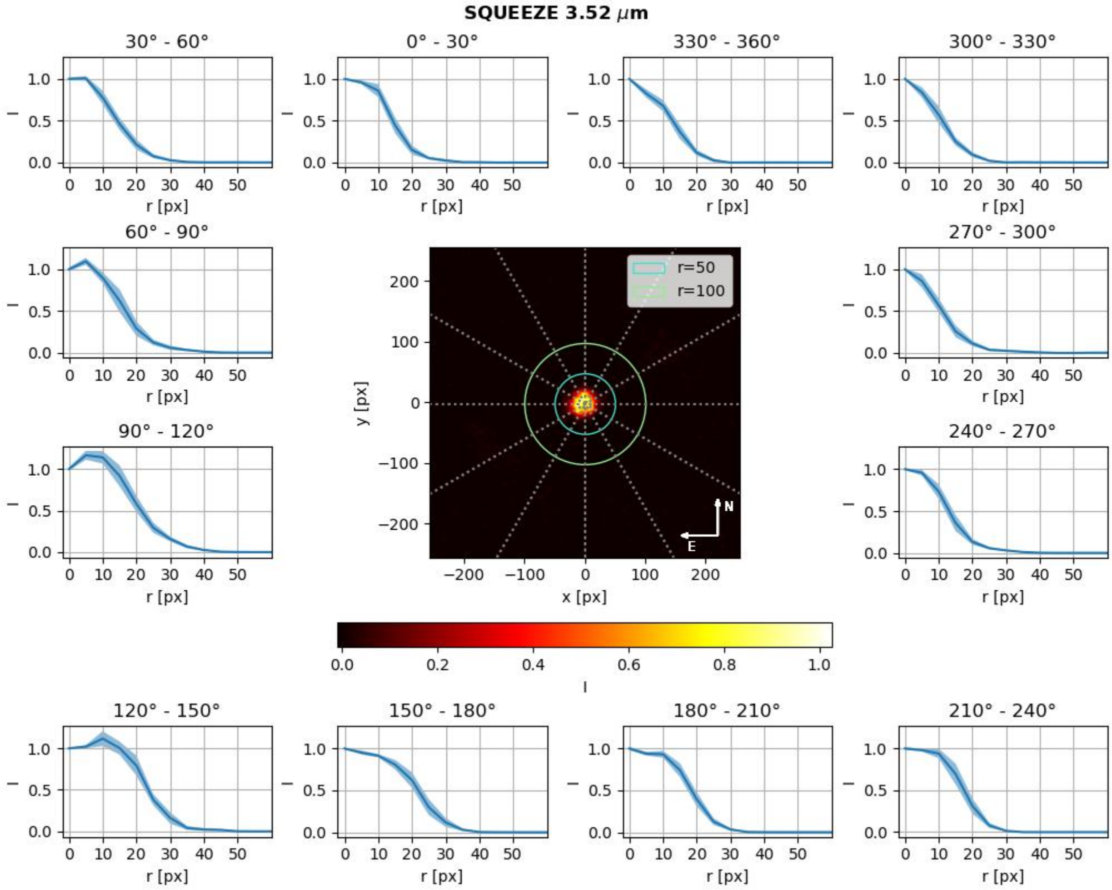

Figure 5.10.: R Scl 3.52 μm merged radial profiles SQUEEZE

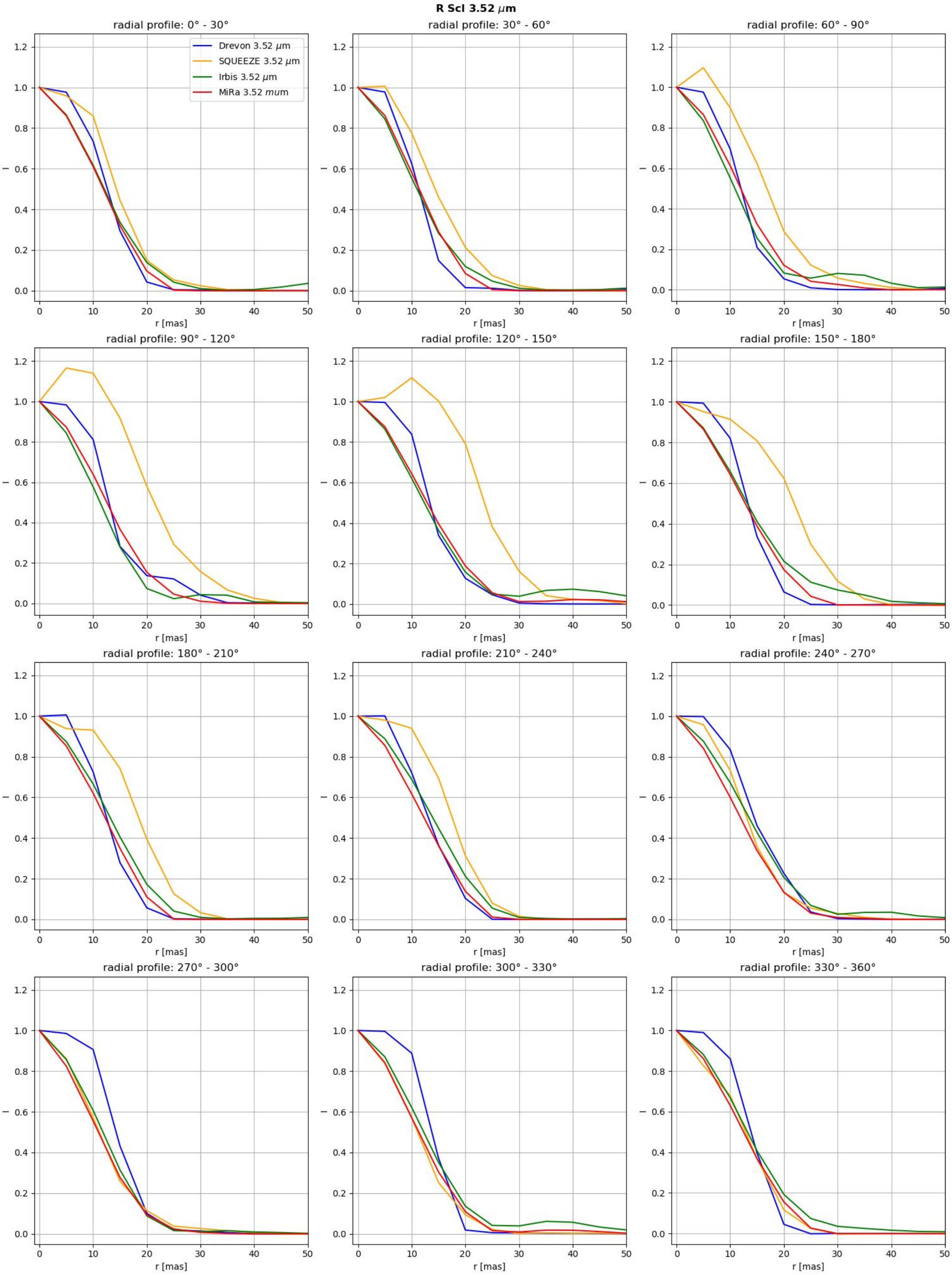

Figure 5.11.: R Scl 3.52 μm merged radial profiles ALL

structure is recognizable in the re-reconstructions. The elongated and triangular shape (in 3.1 μm and 3.52 μm respectively), as well as the fainter shell surrounding the central component are shown. With the exception of SQUEEZE that re-reconstructs a slightly smaller object, all re-reconstructions also fit in size with the input-images. Nevertheless, MiRa reproduces the results best from synthetic data, even the artefacts in the outer corners of the input image are re-reconstructed. Therefore this proves the reproducibility of the reconstruction, leading to the conclusion that the structures seen here are real.

To identify artefacts, the re-reconstructions were also computed based on synthetic data generated from the vertically flipped images (see Figure 5.14 and 5.15). Similar to the previous cases, the images correspond in size and in the overall shape, showing a clear shell around the image. Additionally, the slightly elongated shape, visible at 3.1 μm is well recovered (especially with IRBis), as well as the somewhat triangular shape at 3.52 μm, leading to the conclusion that these results are reliable. To take a deeper look at the environment the images were also displayed in a logarithmic scale (see Figure 5.14b and 5.15b). The faint "blobs" found in the corners of the flipped SQUEEZE and MiRa images (either in 3.1 μm as well as in 3.52 μm) are not re-reconstructed again. Therefore it can be concluded that these background emissions are artefacts and hence are products of the reconstruction process and not real data, at least with the used uv-coverage.

Another interesting structure is found at 3.52 μm in the logarithmic plots of the MiRa reconstructions (see Figure 5.13b).The faint arcs that border directly on the object in the north-west and south-east are reproduced quite well in the re-reconstructed images. In the vertically flipped images these structures are not reproduced, indicating that these are artefacts of the MiRa algorithm. Additionally, one can conclude that MiRa produces artefacts in the north-west south-east direction. This could be due to the angular resolution, which is worse in this direction, seen in both the uv-coverage plot (see Figure 4.5) and the dirty beam (see Figure 5.16).

Of interest is also the fact that IRBis reproduces the artefacts when the image is vertically flipped, in contrast to when it is upright. This suggests that IRBis may reconstruct structures along the north-east to south-west line better than in the other directions. Despite it, these structures are accepted as artefacts, since they are not reproduced in the upright tests.

Since the object in 3.1 μm is elongated from north to south, the re-reconstructed images obtained from the vertically flipped data cannot provide too much information about the significance of the structures seen in the vertical direction. Therefore, the images were rotated by 90 degrees and calculated again (see Figure 5.17 and 5.18). At 3.1 μm the elongated shape that now follows the horizontal axis, as well as the decentered spot (now in the south-east), are reproduced well, especially in SQUEEZE. The triangular shape and the faint shell surrounding the central object, visible in 3.52 μm, are also visible. The logarithmic plots (see Figure 5.17b and 5.18b) show again the artefacts produced by MiRa located in the outer noth-west and south-east regions of the images. The horizontal arcs visible in the 3.52 μm in the MiRa reconstruction are not reproduced. As a conclusion, these features must then be artefacts.

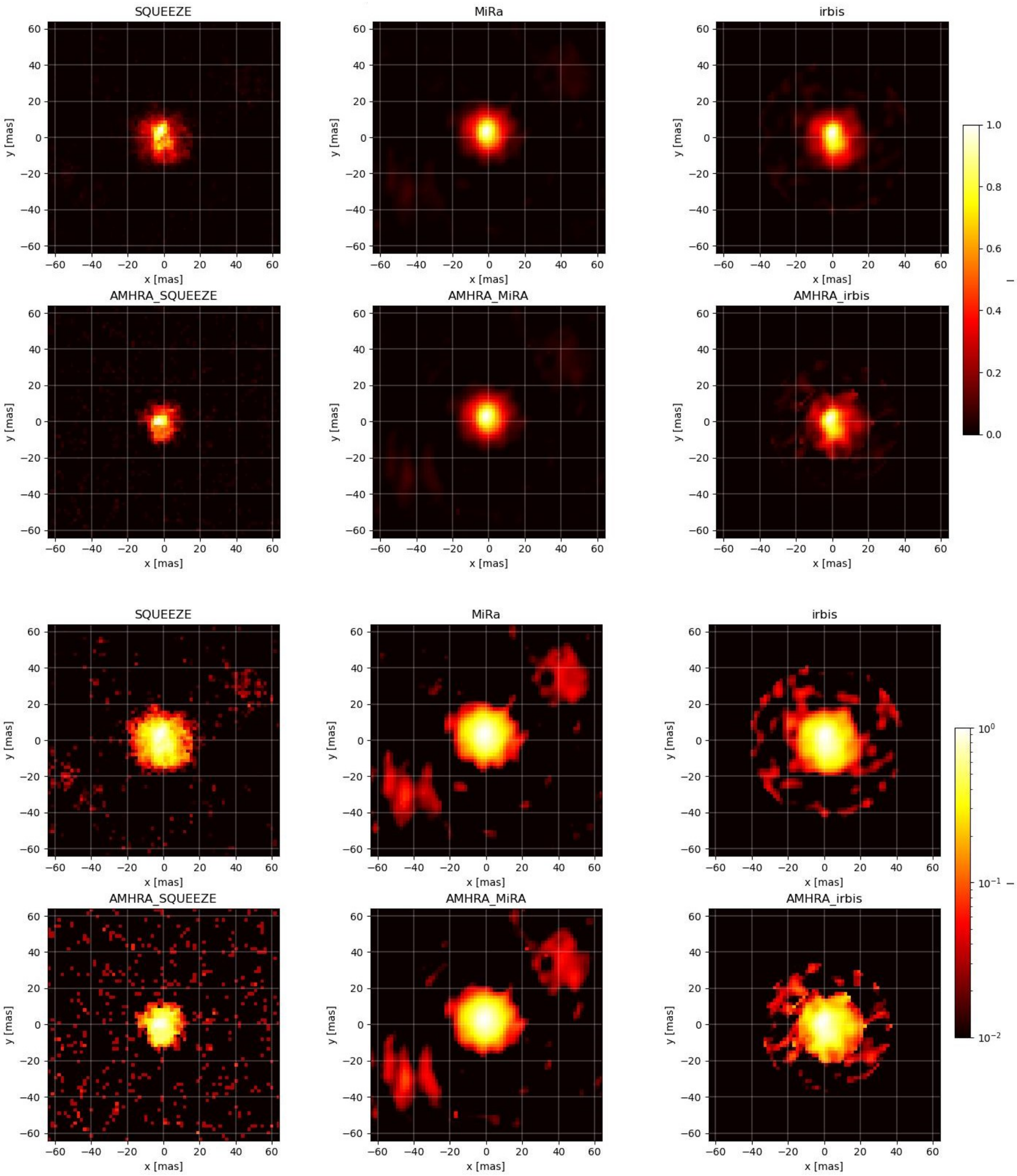

Figure 5.12.: Re-Reconstructions (*bottom rows*) of synthetic observational data generated with AHMRA from the reconstructed images (*top rows*) for 3.1 μm, plotted in a) linear scale, b) logarithmic scale. North is up, East is left (this applies to all subsequent images)

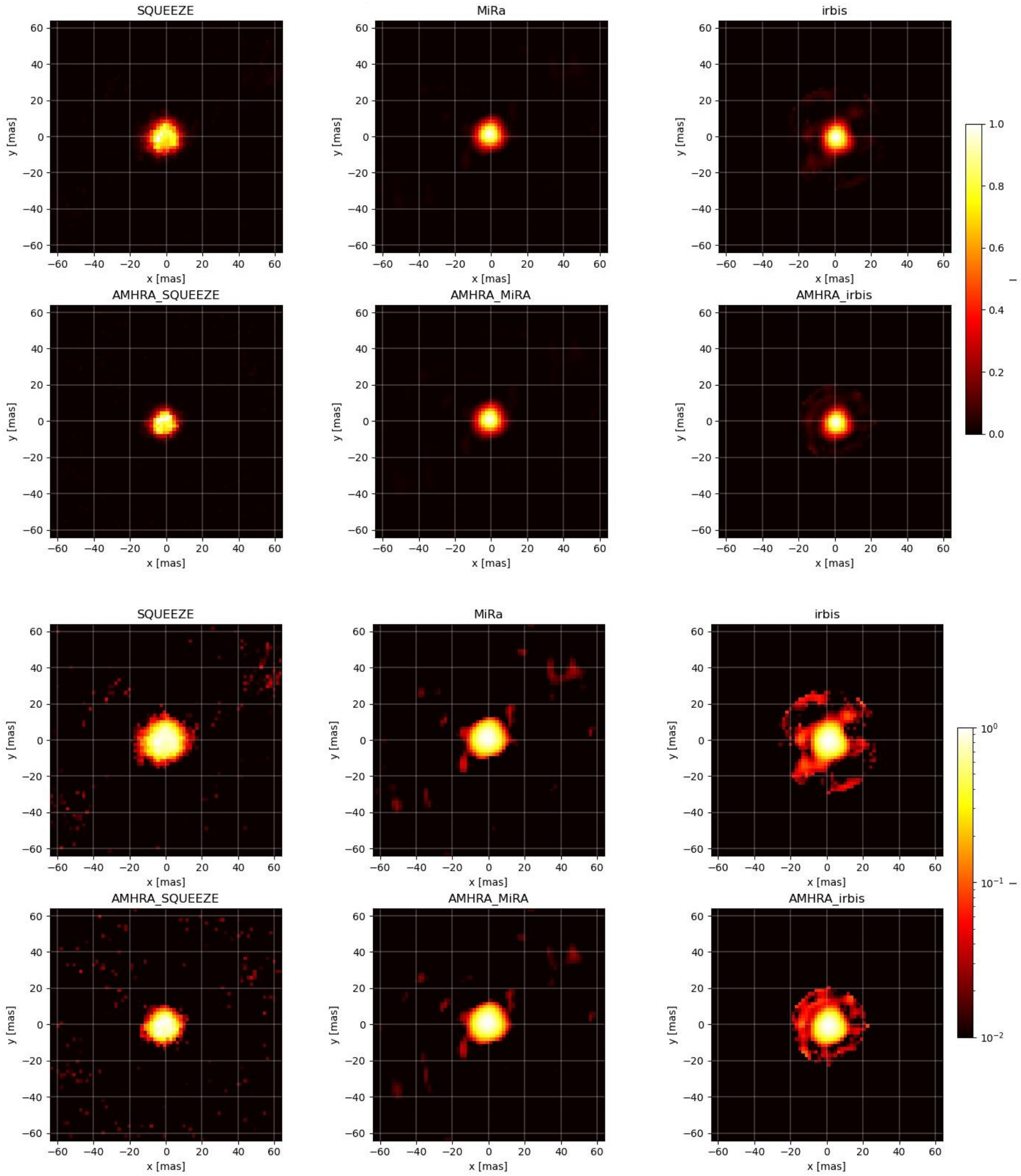

Figure 5.13.: Re-Reconstructions (*bottom rows*) of synthetic observational data generated with AHMRA from the reconstructed images (*top rows*) for 3.52 μm, plotted in a) linear scale, b) logarithmic scale

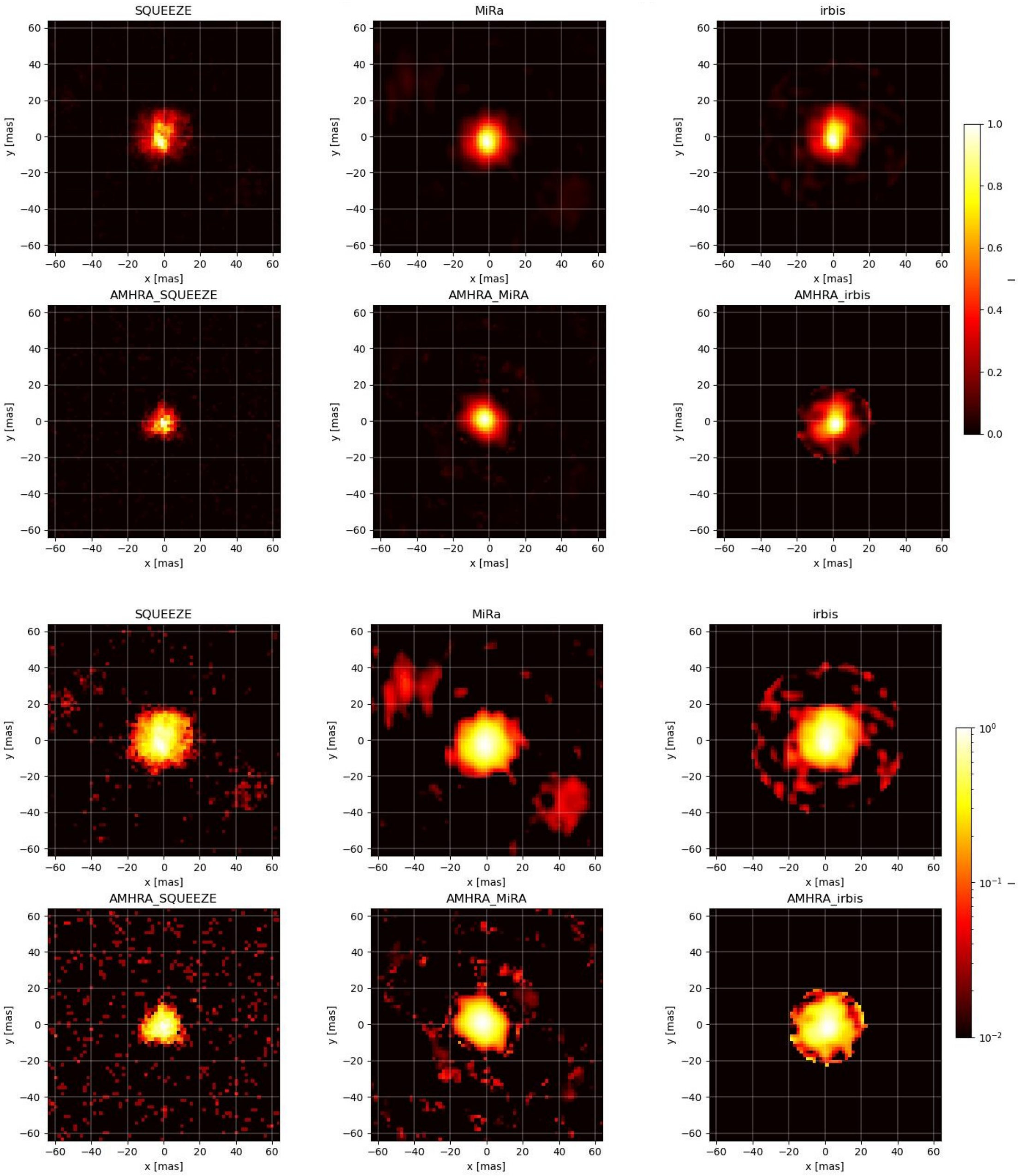

Figure 5.14.: Re-Reconstructions (*bottom rows*) of synthetic observational data generated with AHMRA from the vertically flipped reconstructed images (*top rows*) for 3.1 μm, plotted in a) linear scale, b) logarithmic scale

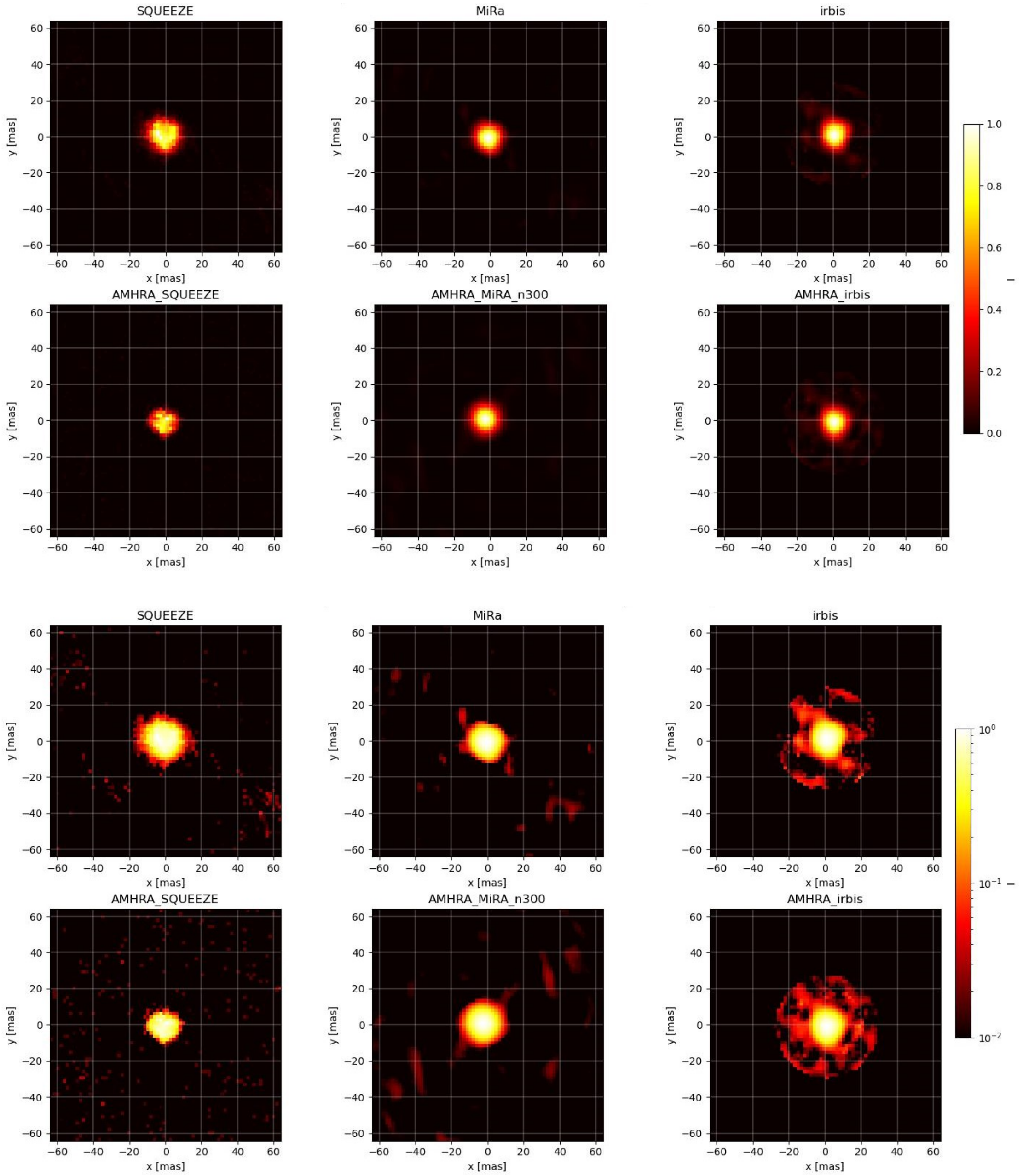

Figure 5.15.: Re-Reconstructions (*bottom rows*) of synthetic observational data generated with AHMRA from the vertically flipped reconstructed images (*top rows*) for 3.52 μm, plotted in a) linear scale, b) logarithmic scale

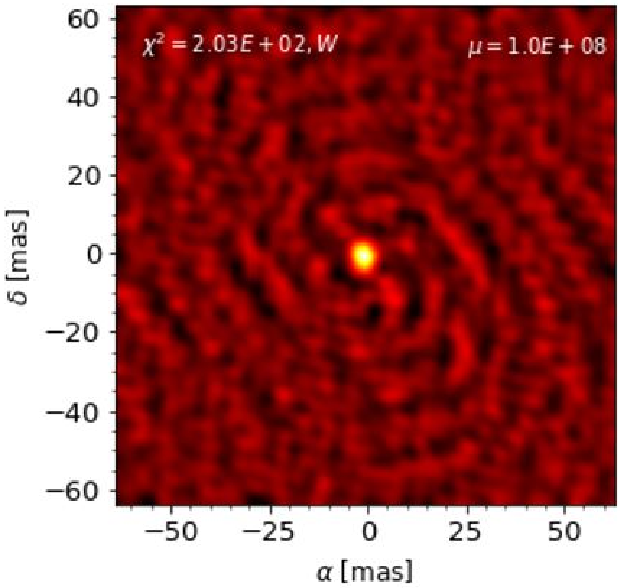

Figure 5.16.: Dirty beam of the R Scl BCD-merged data obtained with MiRa

The results discussed above show that SQUEEZE produces the fewest and weakest artefacts out of the three reconstruction algorithms. MiRa images have strong artefacts along the axis with a less dense uv-coverage and IRBis produces more but scattered high-intensity artefacts in a close surrounding of the central object with some preference along the axis with a denser uv-coverage.

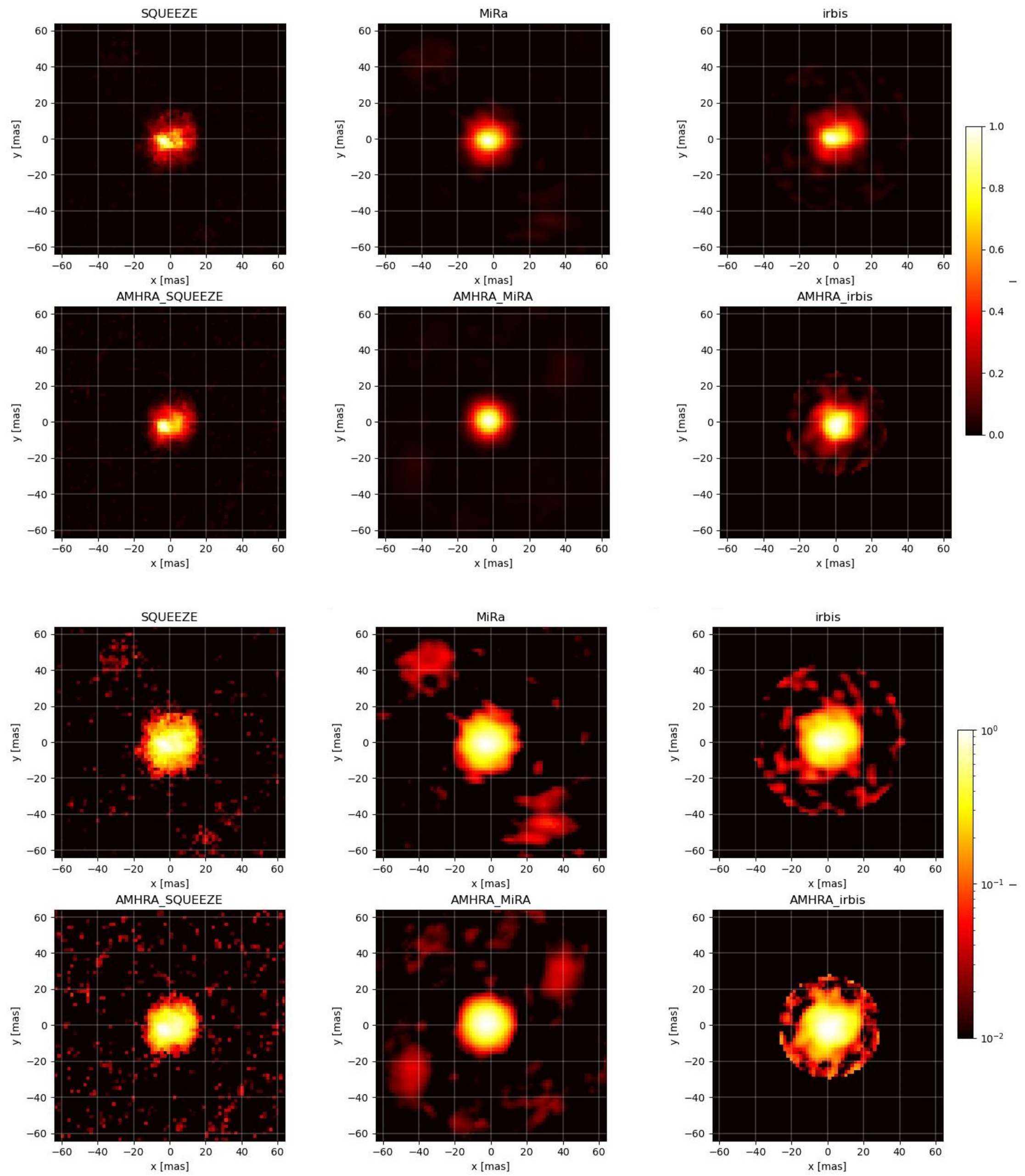

Figure 5.17.: Re-Reconstructions (*bottom rows*) of synthetic observational data generated with AHMRA from the 90° rotated reconstructed images (*top rows*) for 3.1 μm, plotted in a) linear scale, b) logarithmic scale

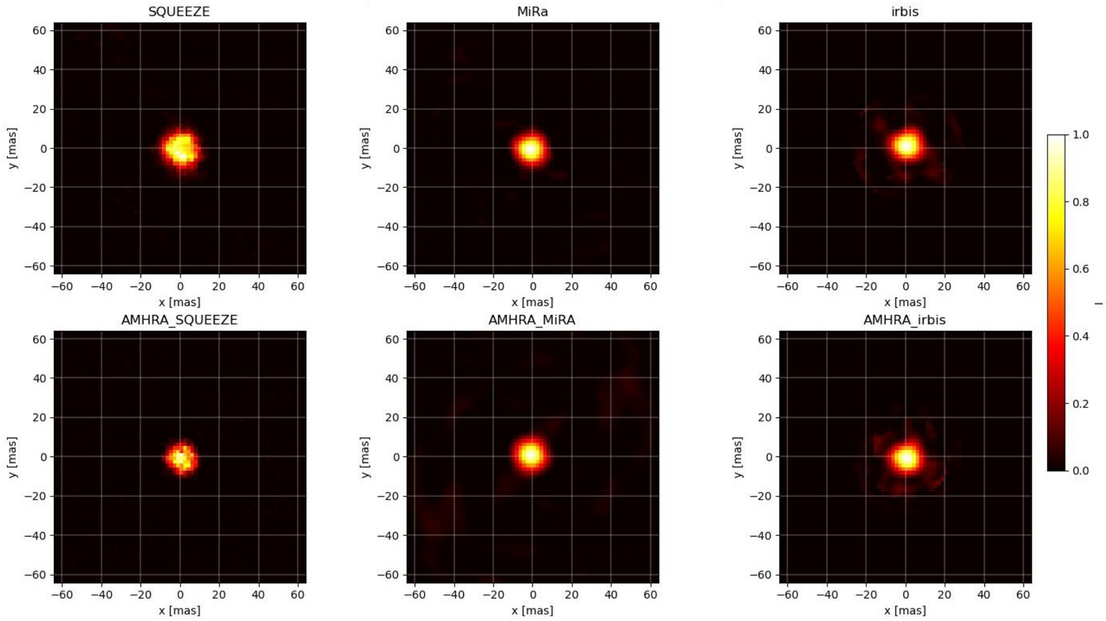

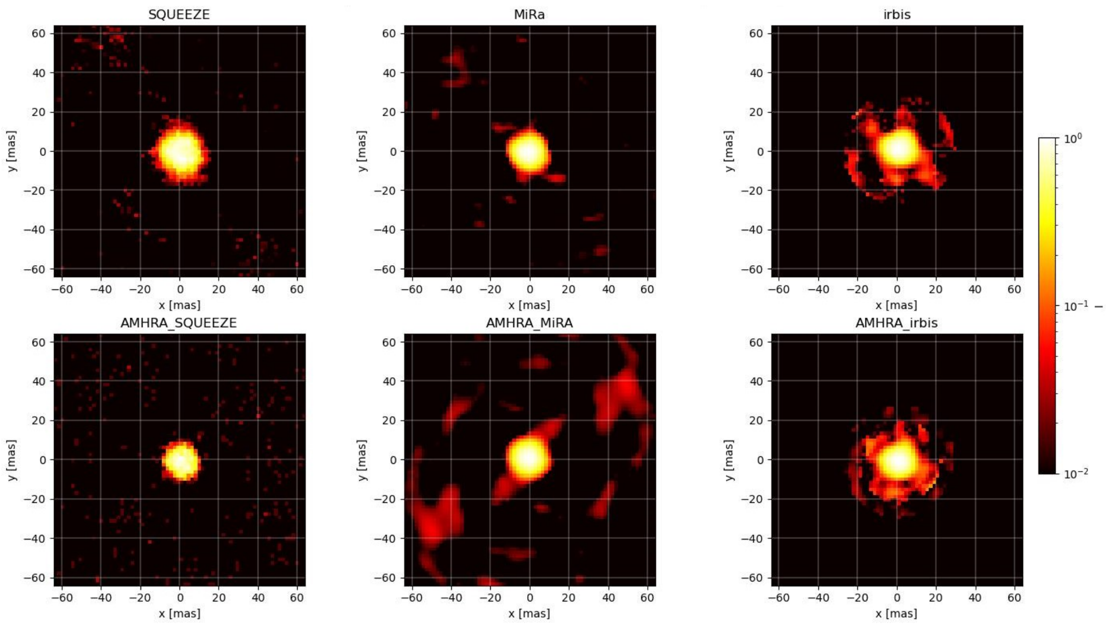

Figure 5.18.: Re-Reconstructions (*bottom rows*) of synthetic observational data generated with AHMRA from the 90° rotated reconstructed images (*top rows*) for 3.52 μm, plotted in a) linear scale, b) logarithmic scale

6. SUMMARY & CONCLUSIONS

AGB stars, such as R Sculptoris, are cool luminous stars at the end of their lives, wrapped by an extended stellar envelope (CSE). Due to internal processes, like thermal pulses (TP) and stellar winds, these stars have a relatively high mass-loss-rate, affecting their evolution. The investigation of such CSEs, their composition and structure is part of current research. R Sculptoris has already been the target of many different investigations ([Olo88], [OME$^+$10], [MMV$^+$12], [MVB$^+$16], [DMC$^+$22], [WHH$^+$17]) which postulate a binary companion, have imaged the surroundings of the star, revealed some information on the composition of the stellar shell and discovered a spiral structure in the CSE.

Stars are very far away, leading to the fact that when they are observed in classical ways, they are seen as point sources. Therefore, interferometry (see Chap. 2) can be used, to reveal surface structures of nearby stars, by reconstructing the recieved observational data to an image (see Chap. 3). It is common to use different image reconstruction algorithms to obtain the most probable results and compare them in terms of morphological structures, intensity profiles or other parameters, as well as artefacts and background noise.

Near-IR data, obtained by the VLTI MATISSE instrument, were reconstructed by using three different image reconstruction methods (SQUEEZE, MiRA and IRBis) within this work.

Overall, all three reconstruction algorithms were able to reconstruct the data, leading to a similar result when compared to each other and the results obtained by Drevon et al. ([DMC$^+$22]).

At $\lambda = 3.1$ μm the calculations revealed a north-south elongated structure with a bright, slightly decentered core, surrounded by a fainter environment, probably the shell. Via radial profile plots the shell was estimated to be at a distance of $\sim$ 5–12 mas from the star.

At $\lambda = 3.52$ μm we can see a marginally triangular shaped structure, settled inside a thin shell, that extends a little bit in the east-west line.

Finally, the reconstructed images were used to generate synthetic observational data and to reconstruct them again. This tests the reproducibility and hence the credibility of the reconstruction algorithm. Hence, the elongated structure and the surrounding faint material at 3.1 μm, as well as the triangular shape at 3.52 μm were assumed to be real.

Artifacts and background noise can be studied by using a flipped or rotated input image to generate the synthetic data. Following this approach, it is surmised that the very faint structures in the corners of the images are artefacts produced by the reconstruction algorithm and therefore are not assumed to be real.

In this study the reproducibility of the structure of R Scl in the near-IR (LM-band) from interferometric data using different image reconstruction methods is tested. Two clear features at 3.1 μm and 3.52 μm were investigated, confirming the results obtained by Drevon et al. ([DMC^{+}22]). Further investigation on the parameters and structure of the CSE of R Scl, as well as the possible time-variability of the AGB-envelope, additional observations at different epochs will be required.

Bibliography

[And07] A. C. Andersen. Dust from AGB Stars. In F. Kerschbaum, C. Charbonnel, and R. F. Wing, editors, *Why Galaxies Care About AGB Stars: Their Importance as Actors and Probes*, volume 378 of *Astronomical Society of the Pacific Conference Series*, page 170, November 2007.

[BMK10] Fabien Baron, John D. Monnier, and Brian Kloppenborg. A novel image reconstruction software for optical/infrared interferometry. In William C. Danchi, Françoise Delplancke, and Jayadev K. Rajagopal, editors, *Optical and Infrared Interferometry II*, volume 7734 of *Society of Photo-Optical Instrumentation Engineers (SPIE) Conference Series*, page 77342I, July 2010.

[DMC+22] J. Drevon, F. Millour, P. Cruzalèbes, C. Paladini, J. Hron, A. Meilland, F. Allouche, K. H. Hofmann, S. Lagarde, B. Lopez, A. Matter, R. Petrov, S. Robbe-Dubois, D. Schertl, P. Scicluna, M. Wittkowski, G. Zins, P. Ábrahám, P. Antonelli, U. Beckmann, P. Berio, F. Bettonvil, A. Glindemann, U. Graser, M. Heininger, Th. Henning, J. W. Isbell, W. Jaffe, L. Labadie, C. Leinert, M. Lehmitz, S. Morel, K. Meisenheimer, A. Soulain, J. Varga, G. Weigelt, J. Woillez, J. C. Augereau, R. van Boekel, L. Burtscher, W. C. Danchi, C. Dominik, V. Gámez Rosas, V. Hocdé, M. R. Hogerheijde, L. Klarmann, E. Kokoulina, J. Leftley, P. Stee, F. Vakili, R. Waters, S. Wolf, and G. Yoffe. Locating dust and molecules in the inner circumstellar environment of R Sculptoris with MATISSE. *Astronomy and Astrophysics*, 665:A32, September 2022.

[EMP23] Frank Eisenhauer, John D. Monnier, and Oliver Pfuhl. Advances in Optical/Infrared Interferometry. *Annual Review of Astron and Astrophysis*, 61:237–285, August 2023.

[GDK+04] A. Glindemann, F. Delplancke, P. Kervella, F. Paresce, A. Richichi, and M. Schöller. Ground interferometric searches (Invited Review). In A. Penny, editor, *Planetary Systems in the Universe*, volume 202, page 417, January 2004.

[Gli11] Andreas Glindemann. *Principles of Stellar Interferometry.* 2011.

[Hab96] H. J. Habing. Circumstellar envelopes and Asymptotic Giant Branch stars. *Astronomy and Astrophysics Reviews*, 7(2):97–207, January 1996.

[HLH+98] J. Hron, R. Loidl, S. Hoefner, U. G. Jorgensen, B. Aringer, and F. Kerschbaum. ISO-SWS spectra of the C-rich AGB star R Scl and dynamical model atmospheres. *Astronomy and Astrophysics*, 335:L69–L72, July 1998.

[HO04] Harm J. Habing and Hans Olofsson. *Asymptotic Giant Branch Stars*. 2004.

[HO18] Susanne Höfner and Hans Olofsson. Mass loss of stars on the asymptotic giant branch. Mechanisms, models and measurements. *Astronomy and Astrophysics Reviews*, 26(1):1, January 2018.

[HWS14] K. H. Hofmann, G. Weigelt, and D. Schertl. An image reconstruction method (IRBis) for optical/infrared interferometry. *Astronomy and Astrophysics*, 565:A48, May 2014.

[KWW13] Rudolf Kippenhahn, Alfred Weigert, and Achim Weiss. *Stellar Structure and Evolution*. 2013.

[LCH+04] P. R. Lawson, W. D. Cotton, C. A. Hummel, J. D. Monnier, M. Zhao, J. S. Young, H. Thorsteinsson, S. C. Meimon, L. Mugnier, G. Le Besnerais, E. Thiebaut, and P. G. Tuthill. The 2004 Optical/IR Interferometry Imaging Beauty Contest. In *American Astronomical Society Meeting Abstracts*, volume 205 of *American Astronomical Society Meeting Abstracts*, page 153.18, December 2004.

[LLP+22] B. Lopez, S. Lagarde, R. G. Petrov, W. Jaffe, P. Antonelli, F. Allouche, P. Berio, A. Matter, A. Meilland, F. Millour, S. Robbe-Dubois, Th. Henning, G. Weigelt, A. Glindemann, T. Agocs, Ch. Bailet, U. Beckmann, F. Bettonvil, R. van Boekel, P. Bourget, Y. Bresson, P. Bristow, P. Cruzalèbes, E. Eldswijk, Y. Fanteï Caujolle, J. C. González Herrera, U. Graser, P. Guajardo, M. Heininger, K. H. Hofmann, G. Kroes, W. Laun, M. Lehmitz, C. Leinert, K. Meisenheimer, S. Morel, U. Neumann, C. Paladini, I. Percheron, M. Riquelme, M. Schoeller, Ph. Stee, L. Venema, J. Woillez, G. Zins, P. Ábrahám, S. Abadie, R. Abuter, M. Accardo, T. Adler, J. Alonso, J. C. Augereau, A. Böhm, G. Bazin, J. Beltran, A. Bensberg, W. Boland, R. Brast, L. Burtscher, R. Castillo, A. Chelli, C. Cid, J. M. Clausse, C. Connot, R. D. Conzelmann, W. C. Danchi, M. Delbo, J. Drevon, C. Dominik, A. van Duin, M. Ebert, F. Eisenhauer, S. Flament, R. Frahm, V. Gámez Rosas, A. Gabasch, A. Gallenne, E. Garces, P. Girard, A. Glazenborg, F. Y. J. Gonté, F. Guitton, M. de Haan, H. Hanenburg, X. Haubois, V. Hocdé, M. Hogerheijde, R. ter Horst, J. Hron, C. A. Hummel, N. Hubin, R. Huerta, J. Idserda, J. W. Isbell, D. Ives, G. Jakob, A. Jaskó, L. Jochum, L. Klarmann, R. Klein, J. Kragt, S. Kuindersma, E. Kokoulina, L. Labadie, S. Lacour, J. Leftley, R. Le Poole, J. L. Lizon, M. Lopez, F. Lykou, A. Mérand, A. Marcotto, N. Mauclert, T. Maurer, L. H. Mehrgan, J. Meisner, K. Meixner, M. Mellein, J. L. Menut, L. Mohr, L. Mosoni, R. Navarro, E. Nußbaum, L. Pallanca, E. Pantin, L. Pasquini, T. Phan Duc, J. U. Pott, E. Pozna, A. Richichi, A. Ridinger, F. Rigal, Th. Rivinius, R. Roelfsema, R. R. Rohloff, S. Rousseau, D. Salabert, D. Schertl, N. Schuhler, M. Schuil, K. Shabun, A. Soulain, C. Stephan, P. Toledo, K. Tristram, N. Tromp, F. Vakili, J. Varga, J. Vinther, L. B. F. M. Waters, M. Wittkowski, S. Wolf, F. Wrhel, and G. Yoffe. MATISSE, the VLTI mid-infrared imaging spectro-interferometer. *Astronomy and Astrophysics*, 659:A192, March 2022.

[Mae16] Matthias Maercker. ALMA observations of the not-so detached shell around the carbon AGB star R Sculptoris. In *Journal of Physics Conference Series*, volume 728 of *Journal of Physics Conference Series*, page 022006, July 2016.

[MMV+12] M. Maercker, S. Mohamed, W. H. T. Vlemmings, S. Ramstedt, M. A. T. Groenewegen, E. Humphreys, F. Kerschbaum, M. Lindqvist, H. Olofsson, C. Paladini, M. Wittkowski, I. de Gregorio-Monsalvo, and L. A. Nyman. Unexpectedly large mass loss during the thermal pulse cycle of the red giant star R Sculptoris. *Nature*, 490(7419):232–234, October 2012.

[MNR12] Thomas Müller-Gronbach, Erich Novak, and Klaus Ritter. *Monte Carlo-Algorithmen*. 2012.

[Mon03] John D. Monnier. Optical interferometry in astronomy. *Reports on Progress in Physics*, 66(5):789–857, May 2003.

[MVB+16] M. Maercker, W. H. T. Vlemmings, M. Brunner, E. De Beck, E. M. Humphreys, F. Kerschbaum, M. Lindqvist, H. Olofsson, and S. Ramstedt. A detailed view of the gas shell around R Sculptoris with ALMA. *Astronomy and Astrophysics*, 586:A5, February 2016.

[Olo88] H. Olofsson. Radio and Infrared Observations of Circumstellar Envelopes. *Space Science Reviews*, 47(1-2):145–174, March 1988.

[OME+10] H. Olofsson, M. Maercker, K. Eriksson, B. Gustafsson, and F. Schöier. High-resolution HST/ACS images of detached shells around carbon stars. *Astronomy and Astrophysics*, 515:A27, June 2010.

[PPJ+24] L. Planquart, C. Paladini, A. Jorissen, A. Escorza, E. Pantin, J. Drevon, B. Aringer, F. Baron, A. Chiavassa, P. Cruzalèbes, W. Danchi, E. De Beck, M. A. T. Groenewegen, S. Höfner, J. Hron, T. Khouri, B. Lopez, F. Lykou, M. Montarges, N. Nardetto, K. Ohnaka, H. Olofsson, G. Rau, A. Rosales-Guzmán, J. Sanchez-Bermudez, P. Scicluna, L. Siess, F. Thévenin, S. Van Eck, W. H. T. Vlemmings, G. Weigelt, and M. Wittkowski. An impressionist view of V Hydrae. When MATISSE paints Asymmetric Giant Blobs. *arXiv e-prints*, page arXiv:2405.07821, May 2024.

[RTM11] S. Renard, E. Thiébaut, and F. Malbet. Image reconstruction in optical interferometry: benchmarking the regularization. *Astronomy and Astrophysics*, 533:A64, September 2011.

[SLO05] F. L. Schöier, M. Lindqvist, and H. Olofsson. Properties of detached shells around carbon stars. Evidence of interacting winds. *Astronomy and Astrophysics*, 436(2):633–646, June 2005.

[STD+16] Joel Sanchez-Bermudez, Eric Thiébaut, Gilles Duvert, Guillaume Mella, John Young, J-Uwe Pott, Nuno Gomes, and Paulo J. V. Garcia. *Reconstruction* *test report and data processing cookbooks, OPTICON FP7-2 Report (JRA.4 deliverable)*. JMMC, Heidelberg, Germany, December 2016. Available at `https://www.jmmc.fr/doc/index.php?search=JRA4Fp7Report2016`.

[Thi08] Eric Thiébaut. MIRA: an effective imaging algorithm for optical interferometry. In Markus Schöller, William C. Danchi, and Françoise Delplancke, editors, *Optical and Infrared Interferometry*, volume 7013 of *Society of Photo-Optical Instrumentation Engineers (SPIE) Conference Series*, page 70131I, July 2008.

[Thi21] Thiébaut, Éric. Quick instructions for using mira. `https://github.com/emmt/MiRA/blob/master/doc/USAGE.md`, 2021. Accessed: 2024-06-04.

[TY17] Éric Thiébaut and John Young. Principles of image reconstruction in optical interferometry: tutorial. *Journal of the Optical Society of America A*, 34(6):904, June 2017.

[WHH+17] M. Wittkowski, K. H. Hofmann, S. Höfner, J. B. Le Bouquin, W. Nowotny, C. Paladini, J. Young, J. P. Berger, M. Brunner, I. de Gregorio-Monsalvo, K. Eriksson, J. Hron, E. M. L. Humphreys, M. Lindqvist, M. Maercker, S. Mohamed, H. Olofsson, S. Ramstedt, and G. Weigelt. Aperture synthesis imaging of the carbon AGB star R Sculptoris. Detection of a complex structure and a dominating spot on the stellar disk. *Astronomy and Astrophysics*, 601:A3, May 2017.

[Wie09] Michael Wiescher. Cosmic alchemy in the laboratory. *Physics Online Journal*, 2:69, August 2009.

A. Appendix

A.1. Radial profiles of R Scl containing the STDV

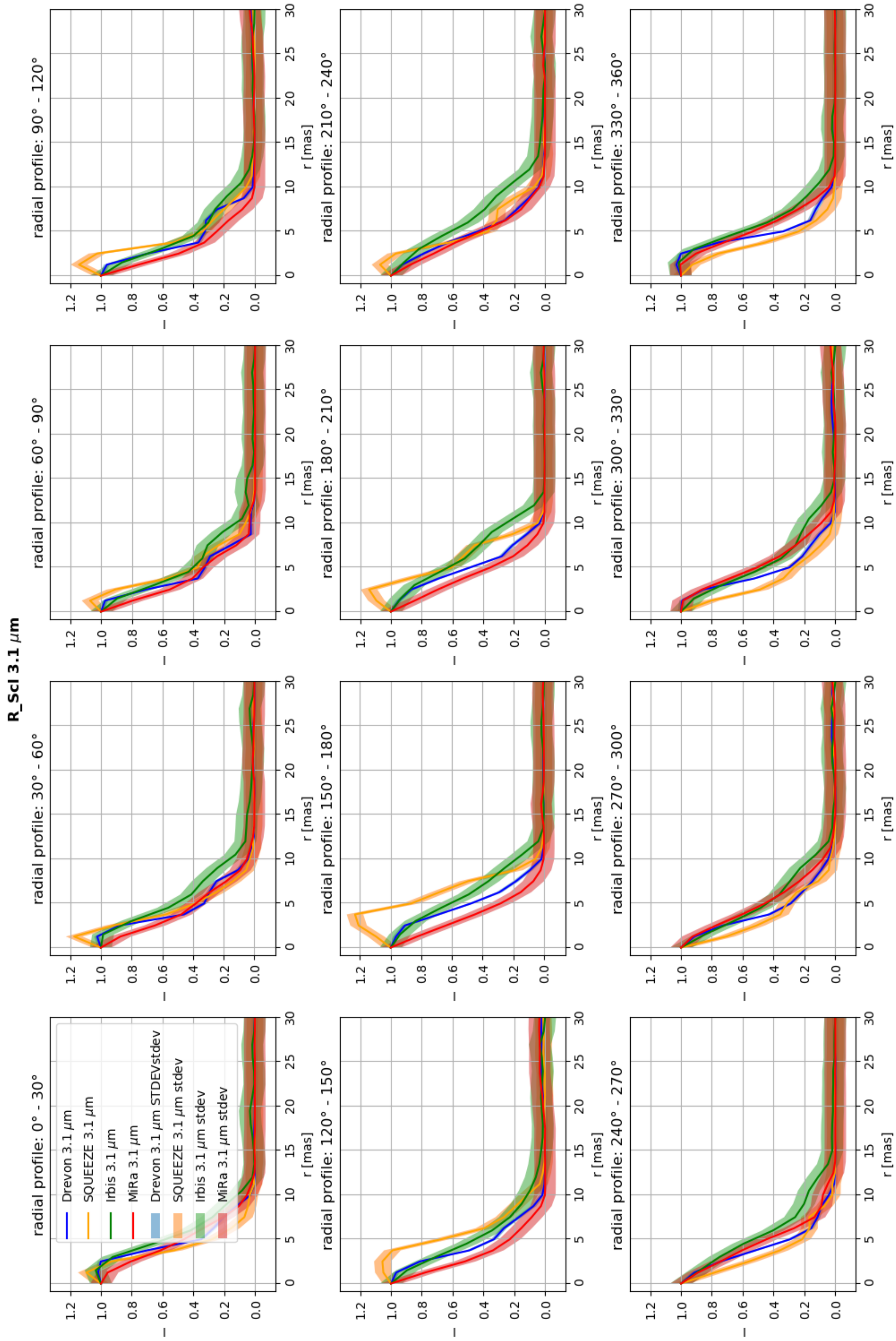

Figure A.1.: R Scl 3.1 μm merged radial profiles ALL including the STDV.

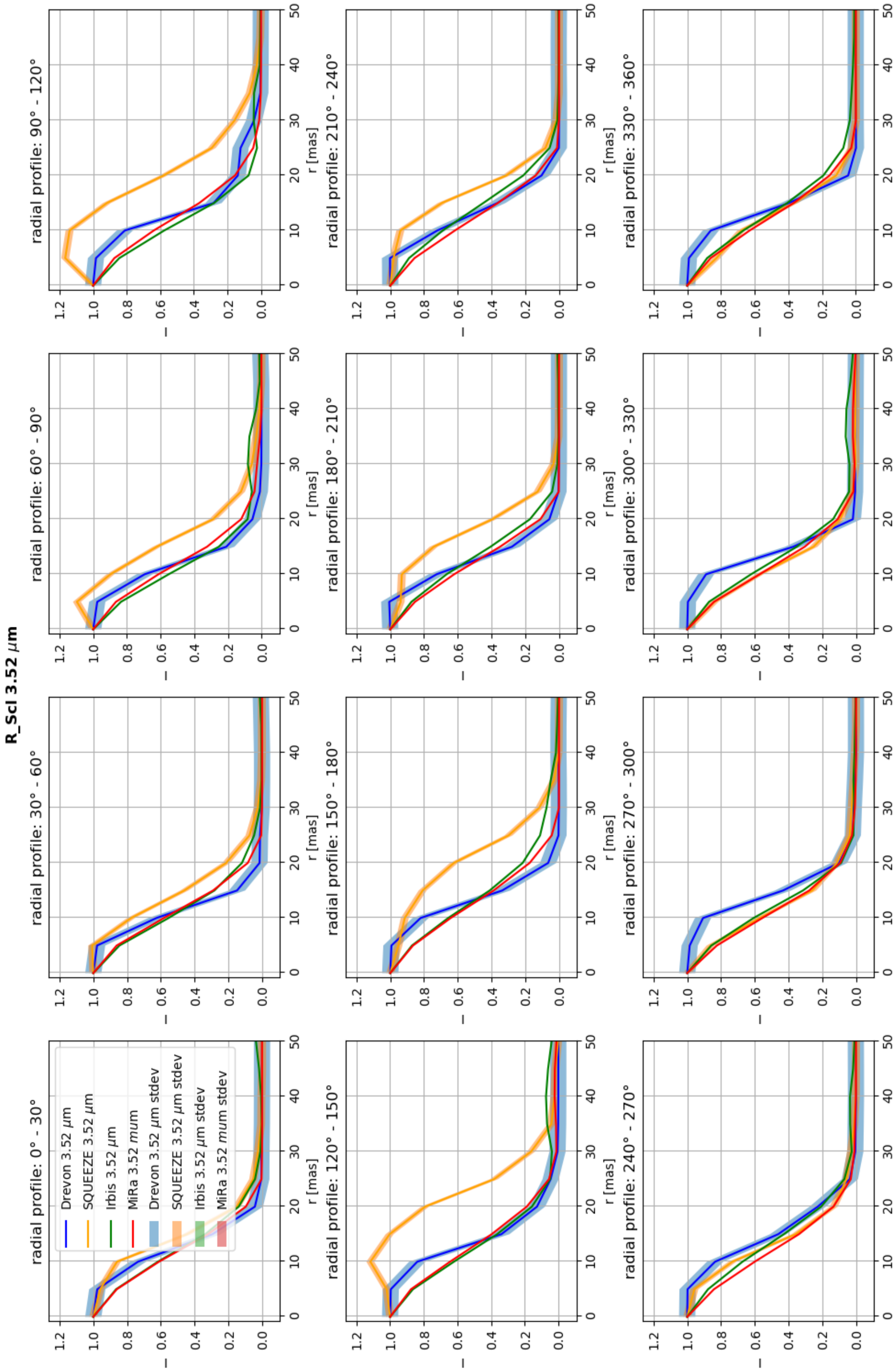

Figure A.2.: R Scl 3.52 μm merged radial profiles ALL including the STDV.